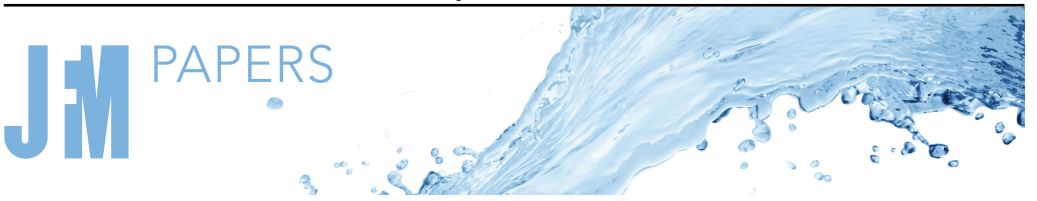
J. Fluid Mech. (2026), *vol.* 1045, A9, doi:10.1017/jfm.2026.12141



Collective migration and diffusion of inertial swimmers under gravity

Yan Xia[1], **Zhaowu Lin**[2], **Zhaosheng Yu**[2] **and Takuji Ishikawa**[1]

[1]Department of Biomedical Engineering, Tohoku University, Sendai 980-8579, Japan

[2]State Key Laboratory of Fluid Power and Mechatronic System, Department of Mechanics, Zhejiang University, Hangzhou 310027, PR China

Corresponding authors: Takuji Ishikawa, t.ishikawa@tohoku.ac.jp; Yan Xia, yan.xia.e3@tohoku.ac.jp

(Received 29 May 2026 UTC; revised 6 August 2026 UTC; accepted 24 August 2026 UTC)

Transport phenomena in swimmer suspensions are ubiquitous in biological environments. In this study, we numerically investigate the transport of swimmers modelled as squirmers in semi-dilute suspensions, with a particular focus on the effects of fluid inertia and sedimentation. In the case of neutrally buoyant swimmers, we demonstrate that the swimmer diffusion can be either suppressed or enhanced with increasing Reynolds number, depending on whether the swimmer behaves as a puller or a pusher. Scaling analysis shows that the diffusion coefficient is inversely proportional to the volume fraction of swimmers in the weakly inertial regime; however, this scaling breaks down as inertia becomes strong. For settling swimmers, we show that sedimentation has only a weak influence on diffusion behaviour at low Reynolds numbers. In contrast, in the moderate-Reynolds-number regime, settling swimmers preferentially reorient opposing gravity, due to fluid-inertial torques. This alignment suppresses the spreading of pushers, while significantly enhancing the settling velocity and vertical diffusion of pullers by promoting the formation of strong vertical structures when the settling effect is strong. Overall, our results highlight the significance of fluid inertia and gravitational sedimentation in regulating transport and collective motion in active suspensions.

Key words: collective behaviour, suspensions, active matter

1. Introduction

Transport phenomena, including diffusion, migration and collective behaviours of biological organisms and engineered artificial swimmers have emerged as central topics in active matter physics and biomedical engineering due to their fundamental importance

© The Author(s), 2026. Published by Cambridge University Press. This is an Open Access article, distributed under the terms of the Creative Commons Attribution licence (https://creativecommons.org/licenses/by/4.0/), which permits unrestricted re-use, distribution and reproduction, provided the original article is properly cited.

https://doi.org/10.1017/jfm.2026.12141 Published online by Cambridge University Press

and wide-ranging applications (Wu *et al.* 2020; Ishikawa 2025). These processes manifest across diverse systems, ranging from collective bacterial swimming and bioconvection to oceanic red tides and microrobot-assisted targeted drug delivery. A better understanding of the transport phenomena of swimmers enables the quantitative prediction of phenomena such as the formation of complex collective structures and the migration dynamics of populations through intricate biological and geophysical environments (Pedley & Kessler 1992; Lauga 2020; Ishikawa *et al.* 2025*b*).

In previous studies, transport phenomena in microswimmer suspensions have been investigated from various perspectives (Ishikawa 2025). The self-diffusion coefficient of microswimmers in the dilute limit has been analytically derived (Berg 1993; Lauga 2020). Early experiments suggest that the large-scale coherent motion observed in bacterial turbulence emerges from hydrodynamic interactions between pushers (Dombrowski *et al.* 2004; Sokolov *et al.* 2007; Zhang *et al.* 2010; Wensink *et al.* 2012; Aranson 2022). Enhanced diffusion of tracers in bacterial turbulence has been observed, where the effective diffusivity can exceed the thermal diffusivity by several orders of magnitude (Wu & Libchaber 2000; Peng *et al.* 2016). Enhanced diffusion induced by the swimming of microalgae has also been observed, where tracer trajectories exhibit rare and large jumps resulting from near collisions with the microalgae (Leptos *et al.* 2009; Jeanneret *et al.* 2016). Numerous studies have investigated the behaviour of swimming microorganisms in various flow fields, including shear flows (Durham *et al.* 2009), Poiseuille flows (Omori *et al.* 2022) and turbulent flows (Durham *et al.* 2013; De Lillo *et al.* 2014; Qiu *et al.* 2022*b*). These studies have highlighted the important role of hydrodynamics in transport phenomena in microswimmer suspensions.

Given the importance of hydrodynamics, the 'squirmer' model, which propels itself through a prescribed surface velocity (Lighthill 1952; Blake 1971; Pedley 2016; Ishikawa 2024), is widely used to investigate full hydrodynamic interactions in swimmer suspensions over a wide range of volume fractions. Using Stokesian dynamics simulations of infinite suspensions, it has been observed that neutral squirmers and weak pullers tend to align and swim in similar directions (Ishikawa *et al.* 2008; Evans *et al.* 2011). Yoshinaga & Liverpool (2018) showed that this polar order is generated by near-field lubrication flow rather than long-range hydrodynamics. Beyond collective motion, hydrodynamic interactions among microswimmers can also give rise to diverse diffusive behaviours. Ishikawa & Pedley (2007*a*) simulated three-dimensional semi-dilute squirmer suspensions and found that translational diffusion of squirmers scales inversely with the volume fraction. Qi *et al.* (2022) reported the rotational diffusion of spheroidal Brownian squirmers in a concentrated regime. The rotational diffusivity exhibited a maximum at an areal fraction of approximately 0.4–0.5. More recently, Ge & Elfring (2025) reported a non-monotonic dependence of the translational diffusion of non-self-propelling squirmers on the volume fraction, with a maximum at $\phi \simeq 0.1$–0.2. For deformable squirmers, membrane deformability has been shown to influence microstructure formation, which in turn modulates microswimmer diffusion in dense suspensions (Kubo *et al.* 2025). Significant progress has also been made in understanding microswimmer transport in complex environments, such as shear flow (Ishikawa 2012; Ge *et al.* 2025), complex fluid (Wang & Ardekani 2015; Ouillon *et al.* 2020; Zhang *et al.* 2024), confinement (Zöttl & Stark 2014; Ishikawa *et al.* 2025*a*) and mixed active–passive suspensions (Chamolly & Ishikawa 2026), highlighting the role of hydrodynamics in microswimmer transport.

Despite substantial progress to date, a complete understanding of swimmer dynamics remains elusive. For one thing, the above results are limited to the vanishing-Reynolds-number regime, where microswimmers are sufficiently small for viscous forces to dominate their dynamics. However, in nature, there exists a wide variety of swimming

https://doi.org/10.1017/jfm.2026.12141 Published online by Cambridge University Press

organisms with diverse sizes and swimming speeds. As the size and swimming speed of a swimmer increase, the Reynolds number correspondingly increases and inertial effects can no longer be neglected. Although the finite-inertia regime has attracted growing attention in recent years, it remains comparatively less explored, particularly regarding transport properties in suspensions. Considerable progress has been made in recent years in understanding the hydrodynamics of a single inertial swimmer (Wang & Ardekani 2012; Khair & Chisholm 2014; Chisholm *et al.* 2016; More & Ardekani 2020; Ouyang *et al.* 2022; Derr *et al.* 2022; Quan *et al.* 2025), where flow inertia plays a significant role in determining the swimming speed and efficiency. Hydrodynamic interactions between pairs of inertial swimmers have also been investigated (Li *et al.* 2016; More & Ardekani 2021; Dombrowski *et al.* 2022). Extensions to many-body systems have subsequently revealed rich collective dynamics in suspensions (Li & Ardekani 2014; Klotsa 2019; Lin & Gao 2019; Ouillon *et al.* 2020). In spite of these advances, the diffusive behaviour of inertial swimmers remains unexplored. Motivated by this gap, this study presents a systematic investigation of swimmer diffusion in the presence of fluid inertia.

Another important point is the effect of gravity. Many microorganisms, such as microalgae and ciliates, exhibit gravitaxis, i.e. a tendency to swim preferentially in the vertical direction in response to gravity (Hemmersbach & Häder 1999). In some microorganisms, this behaviour originates from bottom-heaviness, where the centre of mass is displaced from the geometric centre, giving rise to a restoring gravitational torque that promotes upwards swimming (Pedley & Kessler 1992; Drescher *et al.* 2009). A similar restoring torque may also arise in negatively buoyant microorganisms with asymmetric body shapes (Roberts & Deacon 2002; Kage *et al.* 2020). When such negatively buoyant swimmers collectively migrate upwards under shear flow, the balance between gravitational and hydrodynamic torques drives preferential accumulation of swimmers through gyrotactic focusing. The resulting non-uniform cell distribution may generate an unstable density stratification, ultimately leading to large-scale bioconvection (Kessler 1986; Pedley & Kessler 1992; Croze *et al.* 2017; Bees 2020; Jiang & Chen 2020; Fung 2023). Beyond bioconvection, simplified fluid-dynamics models have been used to investigate gyrotactic swimmers (Ardekani *et al.* 2017; Lovecchio *et al.* 2019; Qiu *et al.* 2022*a*, 2024). In addition, suspensions of settling squirmers confined between two walls have been studied (Kuhr *et al.* 2017; Rühle *et al.* 2022; Barriuso *et al.* 2025), revealing rich collective dynamics arising from the interplay between hydrodynamic interactions and gravity. Although the transport of settling swimmers has been investigated, the effects of fluid inertia on vertical migration, diffusion and microstructure formation are still poorly understood.

As highlighted previously, fluid inertia and sedimentation can influence swimmer transport. Motivated by these prior findings, we conducted direct numerical simulations of swimmer suspensions to elucidate the respective contributions of fluid inertia and gravitational sedimentation to the swimmer dynamics. Specifically, we consider semi-dilute suspensions of spherical squirmers at volume fractions from 0.025 to 0.1. We neglect bottom-heaviness, shape asymmetry and Brownian motion, thereby allowing us to identify inertia and sedimentation-induced mechanisms unambiguously. In § 2, we describe the mathematical formulation, the governing equations and the simulation set-up. In § 3, we provide some validations of the numerical method. We investigate the diffusive behaviour of neutrally buoyant swimmers in § 4. The effects of the swimming Reynolds number on the diffusive properties are demonstrated, and the scaling behaviour is discussed. In § 5, the effects of sedimentation on vertical migration, anisotropic diffusion and microstructure of settling swimmers are examined. Finally, we conclude the study in § 6.

https://doi.org/10.1017/jfm.2026.12141 Published online by Cambridge University Press

2. Mathematical formulation and simulation set-up

2.1. *Squirmer model*

We consider spherical swimmers that propel themselves by generating tangential velocities along their surface, known as a squirmer. For each swimmer, the surface velocity is given by (Lighthill 1952; Blake 1971; Ishikawa *et al.* 2006)

$$\boldsymbol{u}_s = B_1\,(\sin\theta + \beta\sin\theta\cos\theta)\,\boldsymbol{e}_\theta, \tag{2.1}$$

where $\theta = \cos^{-1}(\boldsymbol{p}\cdot\boldsymbol{r}/r)$ represents the polar angle between the position vector $\boldsymbol{r}$, measured from the particle's centre, and the swimming direction $\boldsymbol{p}$, while $\boldsymbol{e}_\theta$ is the unit tangent vector along the θ direction. Throughout this work, we fix B_1 which determines the swimming speed of a solitary squirmer in the Stokes regime, where $V_s = 2B_1/3$, which is independent of β. The squirmer parameter β regulates the strength of the force dipole generated by the swimmer and determines whether the squirmer behaves as a puller ($\beta > 0$) or a pusher ($\beta < 0$). Furthermore, in the present study, we neglect bottom-heaviness of the squirmer and assume that the centre of mass coincides with the centre of the sphere.

2.2. *Basic equations*

The transport of swimmers in a fluid is simulated by direct numerical solution of the Navier–Stokes equations using the fictitious domain method (Yu & Shao 2007). Here, we briefly describe the basic equations; details of the method can be found in Lin & Gao (2019). Let Ω and P represent the entire domain and the domain occupied by the swimmers, respectively ($P \subset \Omega$). Here P is bounded by the swimmer surface S.

The flow is governed by the Navier–Stokes equations,

$$\rho_f \frac{\mathrm{d}\boldsymbol{u}}{\mathrm{d}t} = \boldsymbol{\nabla}\cdot(-p\boldsymbol{I} + \boldsymbol{\tau}) + \boldsymbol{f} \quad \text{in} \quad \Omega. \tag{2.2}$$

$$\boldsymbol{\nabla}\cdot\boldsymbol{u} = \boldsymbol{0} \quad \text{in} \quad \Omega. \tag{2.3}$$

The velocity boundary condition on swimmer surface is given by

$$\boldsymbol{u} = (\boldsymbol{U} + \boldsymbol{\omega}\times\boldsymbol{r}) + \boldsymbol{u}_s \quad \text{in} \quad S. \tag{2.4}$$

Here, $\boldsymbol{u}$, p and ρ_f represent the fluid velocity, pressure and density, respectively. The stress tensor $\boldsymbol{\tau} = 2\mu\dot{\boldsymbol{\gamma}}$, where μ is the viscosity and $\dot{\boldsymbol{\gamma}}$ is the strain rate tensor. The body force $\boldsymbol{f}$ accounts for the fluid–particle interaction defined in the particle domain.

Next, we describe the motion of spherical swimmers with density ρ_s and radius a. The swimmer velocity $\boldsymbol{U}$ and angular velocity $\boldsymbol{\omega}$ obey Newton's equations of motion,

$$\rho_s V_p \frac{\mathrm{d}\boldsymbol{U}}{\mathrm{d}t} = \int_S \boldsymbol{n}\cdot(-p\boldsymbol{I} + \boldsymbol{\tau})\ \mathrm{d}s + (\rho_s - \rho_f)V_p\boldsymbol{g}, \tag{2.5}$$

$$\frac{\mathrm{d}\,(\boldsymbol{J}\cdot\boldsymbol{\omega})}{\mathrm{d}t} = \int_S \boldsymbol{r}\times\left[\boldsymbol{n}\cdot(-p\boldsymbol{I} + \boldsymbol{\tau})\right]\ \mathrm{d}s. \tag{2.6}$$

Here, V_p and $\boldsymbol{J}$ denote the swimmer volume and the moment of inertia tensor, respectively. The vector $\boldsymbol{r}$ is measured relative to the particle centre of mass, and $\boldsymbol{g}$ denotes the gravitational acceleration.

The position of each swimmer, $\boldsymbol{x} = (x, y, z)^T$, is determined from the following kinematic equation:

$$\frac{\mathrm{d}\boldsymbol{x}}{\mathrm{d}t} = \boldsymbol{U}. \tag{2.7}$$

https://doi.org/10.1017/jfm.2026.12141 Published online by Cambridge University Press

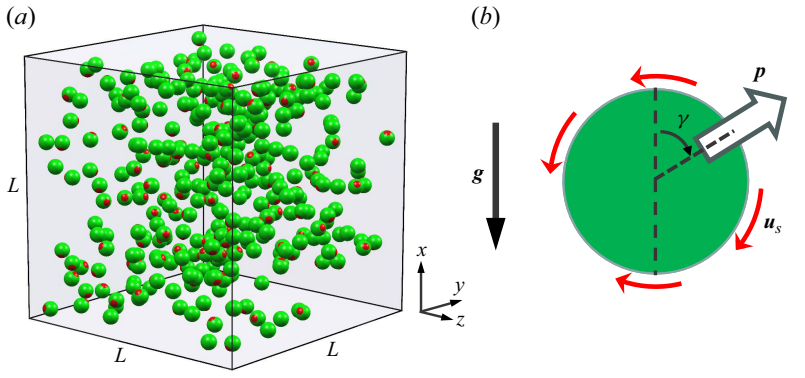


Figure 1. Schematic representation of the model system. (*a*) Simulation set-up of the suspension. (*b*) Sketch of a squirmer, where γ is the angle between the orientation vector $\boldsymbol{p}$ and the positive x-axis.

To accurately capture the orientation of swimmers, we employ a body-fixed coordinate system (x', y', z'), which is aligned with the swimmer's centre, with the z'-axis pointing in the direction of swimming, denoted as $\boldsymbol{p}$. The swimmer orientation is determined by

$$\frac{\mathrm{d}\boldsymbol{q}}{\mathrm{d}t} = \frac{1}{2}\begin{pmatrix} q_4 & -q_3 & q_2 & q_1 \\ q_3 & q_4 & -q_1 & q_2 \\ -q_2 & q_1 & q_4 & q_3 \\ -q_1 & -q_2 & -q_3 & q_4 \end{pmatrix}\begin{pmatrix} \omega_x' \\ \omega_y' \\ \omega_z' \\ 0 \end{pmatrix}. \tag{2.8}$$

In (2.8), q_1, q_2, q_3 and q_4 are the components of the unit quaternion $\boldsymbol{q}$, which can be defined in terms of the Euler angles (Yu & Shao 2007). The components of the angular velocity, ω_x', ω_y' and ω_z', are measured in the body-fixed frame. With the quaternion $\boldsymbol{q}$, the rotation matrix from the space-fixed frame to the body-fixed frame is

$$\boldsymbol{R} = 2\begin{pmatrix} q_1^2+q_4^2-\frac{1}{2} & q_1q_2+q_3q_4 & q_1q_3-q_2q_4 \\ q_1q_2-q_3q_4 & q_2^2+q_4^2-\frac{1}{2} & q_2q_3+q_1q_4 \\ q_1q_3+q_2q_4 & q_2q_3-q_1q_4 & q_3^2+q_4^2-\frac{1}{2} \end{pmatrix}. \tag{2.9}$$

Since the swimmer is rotationally symmetric, its orientation $\boldsymbol{p}$ is fully determined by the direction of its symmetry axis, the z' axis, in the space-fixed frame. orientation vector is given by $\boldsymbol{p} = \boldsymbol{R}\cdot(0,\,0,\,1)^T$.

The computational code has been extensively validated for the dynamics of squirmers at low Reynolds numbers (Xia *et al.* 2025*b*,*c*), as well as for the sedimentation of a single sphere (Yu & Shao 2007; Xia *et al.* 2022). Validations covering squirmer dynamics in the inertial regime and the hindered settling of passive spheres are presented in § 3.

2.3. *Simulation set-up*

As delineated in figure 1, we consider a suspension of N spherical swimmers with radius a in a periodic cubic domain of side length L, yielding a volume fraction of swimmers $\phi = 4\pi Na^3/(3L^3)$. For the simulations presented in this work, the computational domain of size $L = 32a$ is discretised on a fixed Cartesian grid with $N_m = 512$ mesh points in each direction, corresponding to 32 grid points across the swimmer diameter (i.e. $2a/\Delta = 32$),

https://doi.org/10.1017/jfm.2026.12141 Published online by Cambridge University Press

which is sufficient to accurately resolve the hydrodynamic interactions between squirmers. The volume fraction of swimmers (ϕ) ranges from 0.025 to 0.1, corresponding to a total number of swimmers ranging from 196 to 782. Initially, the swimmers are randomly distributed in space with random orientations. The effect of the domain size L has been examined numerically in Appendix B. In the simulations, zero-volume-flux condition $(\phi\langle \boldsymbol{U}\rangle + (1-\phi)\langle \boldsymbol{u}\rangle = \boldsymbol{0}$, with $\langle\cdot\rangle$ denoting an instantaneous average over all particles or fluid nodes) is imposed via a dynamically adjusted pressure gradient. All computations were normalised by using the swimmer radius a for length, V_s for velocity, a/V_s for time, $\mu V_s/a$ for stress and $\mu V_s/a^2$ for body force. We treat the steric interaction between swimmers by adding an inter-particle repulsive force (Ishikawa *et al.* 2008) in order to avoid the overlap of swimmers. The time step in all simulations is set to $\Delta t = 10^{-3}a/V_s$. Each simulation is run for a total duration of $2500a/V_s$ to ensure that the measured quantities were fully converged.

Fluid inertia is characterised by the swimming Reynolds number

$$Re_S = \frac{\rho_f V_s a}{\mu}, \tag{2.10}$$

which represents the ratio between the inertial force of the fluid and the viscous force due to swimming. Owing to their small size, most microorganisms swim in the Stokes regime, where fluid inertia is negligible. However, in nature, there exists a wide variety of swimming organisms. For instance, the millimetre-sized copepods and *Pleurobrachia* commonly achieve Re_S up to $O(10)$ (Kiørboe *et al.* 2010). Motivated by such examples, we investigate the hydrodynamic diffusion of swimmers with $0.01 \leqslant Re_S \leqslant 10$, covering regimes of both negligible and finite fluid inertia.

The numerical cases are further classified into neutrally buoyant swimmers and settling swimmers, depending on whether a density mismatch exists between the swimmer and the surrounding fluid. To isolate the effects of fluid inertia and sedimentation, Brownian motion and bottom-heaviness are neglected in the present study. The density of microswimmers is usually close to that of the background fluid. For neutrally buoyant swimmers, the density ratio ρ_s/ρ_f is equal to unity; therefore, they do not settle under gravity. For settling swimmers, ρ_s/ρ_f is chosen as 1.02 to reflect the small density mismatch commonly found in natural aquatic microorganisms. The gravitational direction is taken in the negative x direction, i.e. $\boldsymbol{g} = -\boldsymbol{e}_x g$, with $g = \|\boldsymbol{g}\|$. The ratio of the settling velocity of a sphere to the swimming velocity of a solitary squirmer in the Stokes limit will be an important parameter to quantify the settling effect. For a spherical particle, the Stokes settling velocity is given by

$$V_g = \frac{2\left(\rho_s - \rho_f\right) g a^2}{9\mu}. \tag{2.11}$$

It should be noted that the actual fall velocity of dilute spherical particles in a periodic domain is smaller than V_g due to the fluid inertial and finite-domain effect. We refer to $\alpha = V_g/V_s$ as the settling coefficient, and $\alpha = 0$ corresponds to the neutrally buoyant cases. Finally, the settling Reynolds number is defined as

$$Re_G = \frac{\rho_f V_g a}{\mu}, \tag{2.12}$$

which can also be expressed as $Re_G = \alpha Re_S$. We restrict $\alpha \leqslant 1$ (i.e. $V_s \geqslant V_g$) to ensure that self-propulsion dominates over gravitational settling. When $\alpha \gg 1$, gravitational settling overwhelms the swimming; such conditions are beyond the scope of the present study. The squirmer parameter was set to $\beta = \pm 5$, motivated by previous studies reporting

https://doi.org/10.1017/jfm.2026.12141 Published online by Cambridge University Press

Parameter name	Symbol	Definition	Values
Swimming Reynolds number	Re_S	$\rho_f V_s a/\mu$	0.01 to 10
Volume fraction	ϕ	$4\pi Na^3/(3L^3)$	0.025 to 0.1
Squirmer parameter	β	B_2/B_1	5 and –5
Density ratio	ρ_s/ρ_f	ρ_s/ρ_f	1 and 1.02
Settling coefficient	α	V_g/V_s	0 to 1

Table 1. List of the non-dimensional parameters.

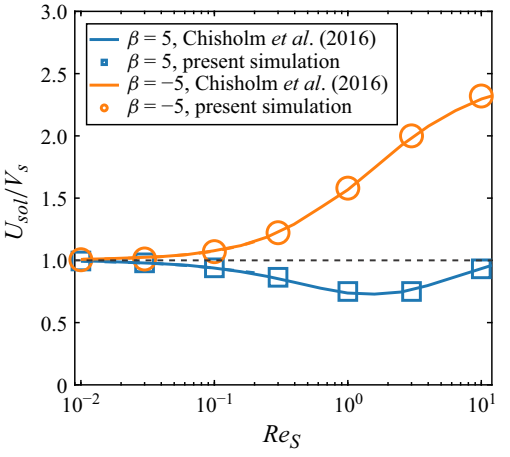


Figure 2. Swimming speed of a solitary squirmer, U_{sol}, as a function of Re_S. Here, U_{sol} is normalised by V_s. The symbols represent our simulation results and lines show the result of Chisholm *et al.* (2016).

qualitative differences between strong pullers and pushers. The definitions and values of non-dimensional parameters are summarised in table 1.

3. Validation

We attempt to validate the accuracy of the solver via three test problems: (a) steady speed of a solitary squirmer across Reynolds numbers; (b) pairwise trajectories of two pullers swimming in opposite directions; (c) hindered settling of passive spheres in a triply periodic box. Case (a) allows us to examine the effect of the Reynolds number on swimming, case (b) enables us to investigate the near-field interaction between two swimmers and case (c) serves to verify the computational accuracy for an infinite settling suspension. The simulation set-ups are identical to those of the suspension cases in § 2.3, unless otherwise specified.

3.1. *Single-swimmer speed*

As reported by Wang & Ardekani (2012) and Chisholm *et al.* (2016), below a critical Reynolds number, a single squirmer exhibits a steady swimming speed U_{sol}, which depends on both β and Re_S. The calculated steady swimming speed U_{sol} versus Re_S with $\beta = \pm 5$ for $Re_S \leqslant 10$ is shown in figure 2. Pushers exhibit a monotonic increase in swimming speed with increasing Re_S, exceeding twice the Stokes-regime value at $Re_S = 10$. In contrast, pullers show a decrease in speed for $Re_S \lesssim O(1)$. As Re_S increases

https://doi.org/10.1017/jfm.2026.12141 Published online by Cambridge University Press

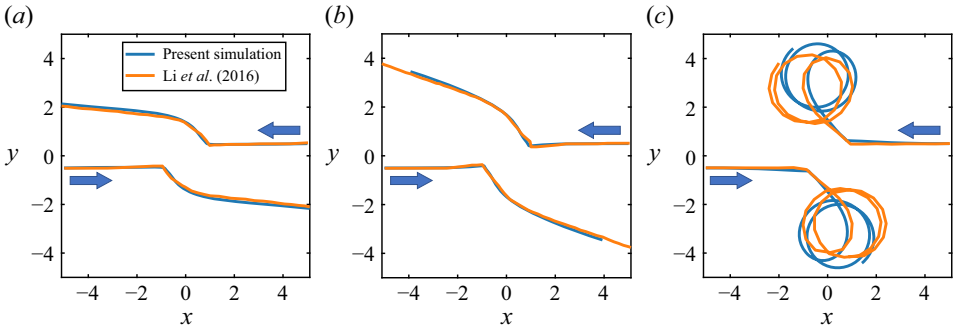


Figure 3. Trajectories of two pullers ($\beta = 5$) swimming in opposite directions at different Reynolds numbers: (*a*) $Re_S = 0.1$, (*b*) $Re_S = 1$ and (*c*) $Re_S = 10$.

beyond $O(1)$, the speed increases. Our results are in good agreement with the numerical results of Chisholm *et al.* (2016) using the spectral element method.

3.2. *Trajectories of a swimmer pair*

Two-body hydrodynamic interactions play a dominant role in transport of swimmers in semi-dilute suspensions. Figure 3 compares the trajectories of two pullers ($\beta = 5$) obtained from our simulations with the results reported by Li *et al.* (2016). The two swimmers are initially located in the same plane ($z = 0$). They initially swim towards each other, and their swimming orientations are initially parallel. They are initially positioned with a centre-to-centre distance of $10a$ along the x-axis and a along the y-axis. As shown in figure 3(*a*,*b*), at $Re_S = 0.1$ and 1, the pullers rotate away from each other during the interaction and eventually escape with positive scattering angles. The scattering angle at $Re_S = 1$ is larger than that at $Re_S = 0.1$. In figure 3(*c*), the pullers become hydrodynamically entrapped near each other, rotating along circular trajectories at $Re_S = 10$. Our simulation results are in agreement with the numerical values reported by Li *et al.* (2016). The validation is limited to pullers because, at Reynolds numbers of order unity, pushers develop intrinsically three-dimensional trajectories after close contact due to the amplification of out-of-plane perturbations. Consequently, the reference results do not provide a suitable benchmark for quantitative comparison.

3.3. *Hindered settling velocity of passive spheres*

The hindered settling of spherical particles is a classical and extensively studied problem. We compare our simulations with previous models and simulations for the average settling speed of randomly distributed non-Brownian spheres in the low-Reynolds-number regime. The Richardson–Zaki correlation $U_{sed}/V_g = (1-\phi)^n$ (Richardson & Zaki 1997) summarises experimental data, and its validity has been confirmed in numerical simulations (Cunha *et al.* 2002) and experiments (Nicolai *et al.* 1995); the Hayakawa–Ichiki model $U_{sed}/V_g = (1-\phi)^3/(1+2\phi+1.429\phi(1-\phi)^3)$ (Hayakawa & Ichiki 1995) has been favourably compared against simulations for a wide range of volume fractions (Padding & Louis 2004).

In figure 4, numerical results from current simulations for passive spheres at low Re_G in a triply periodic cubic box of size $L = 32a$ are plotted as a function of the volume fraction. The average settling speed decreases as the particle volume fraction increases due to the hindered effect. Our simulation results lie between the predictions of the Richardson–Zaki correlation and the Hayakawa–Ichiki model. The simulated speed for $\phi = 0.025$ is

https://doi.org/10.1017/jfm.2026.12141 Published online by Cambridge University Press

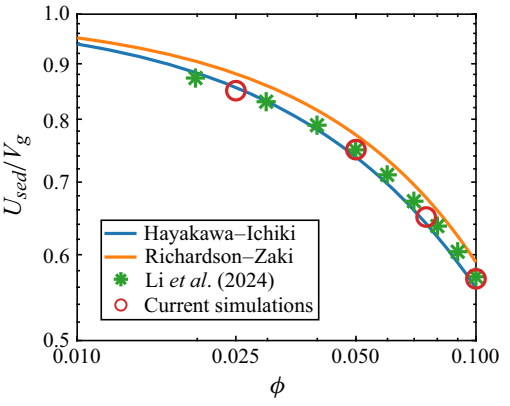


Figure 4. Average settling speed of randomly distributed spheres versus volume fraction.

slightly smaller than the values predicted by the models. This is expected because of the use of triply periodic boundary conditions in a finite domain (Phillips *et al.* 1988). Our results also agree well with the simulation results of Li & Botto (2024) using the Stokesian dynamics method with domain size of $L = 56a$.

4. A suspension of neutrally buoyant swimmers

4.1. *Effects of swimming Reynolds number on diffusion*

The diffusion coefficient is a measure of the increasing displacements of particles, which is calculated based on the mean-square displacement (MSD) of particles. In the case of neutrally buoyant swimmers, there is no preferred direction of motion, so particle motion is expected to be isotropic. Thus, we calculate the total MSD by

$$\left\langle \Delta r^2(t) \right\rangle \equiv \left\langle [\boldsymbol{x}(\tau + t) - \boldsymbol{x}(\tau)]^2 \right\rangle, \tag{4.1}$$

where $\boldsymbol{x}(t) = \boldsymbol{x}(t_0) + \int_{t_0}^{t} \boldsymbol{U}(t')\,\mathrm{d}t'$ is the position of a particle at time t and $\langle \cdot \rangle$ is an average over all particles and reference times. If the MSD grows linearly with time, then the spreading is diffusive. The time-dependent diffusivity is defined as

$$D(t) = \frac{\left\langle \Delta r^2(t) \right\rangle}{6t}. \tag{4.2}$$

Then it allows us to evaluate the long-time diffusion coefficient as $D_t = \lim_{t \to \infty} D(t)$.

Before discussing the diffusion coefficient, the MSDs of pullers and pushers at different swimming Reynolds numbers and $\phi = 0.05$ are shown as a log–log plot in figure 5. We see that MSDs grow as $\sim t^2$ for short times and as $\sim t$ for long times in all cases, which confirms a ballistic-to-diffusive transition. Interestingly, the MSDs of pullers decrease with increasing Re_S, whereas for pushers the MSDs increase as Re_S is increased. For the puller suspension at $Re_S = 10$, the MSD oscillates strongly in the intermediate-time regime, resulting in much smaller spreading. This oscillation in the MSD arises from pairwise interactions between pullers (see figure 3*c*). The pullers undergo continuous rotation during near interactions, resulting in a small net displacement over long times. The modified diffusion process is also evident from trajectories of sample swimmers. As illustrated by the insets in figure 5, increasing Re_S renders puller trajectories more circular, while pusher trajectories become more extended and persistent. We note that the damped MSD oscillations share similarities with those observed for swimmers subject to

https://doi.org/10.1017/jfm.2026.12141 Published online by Cambridge University Press

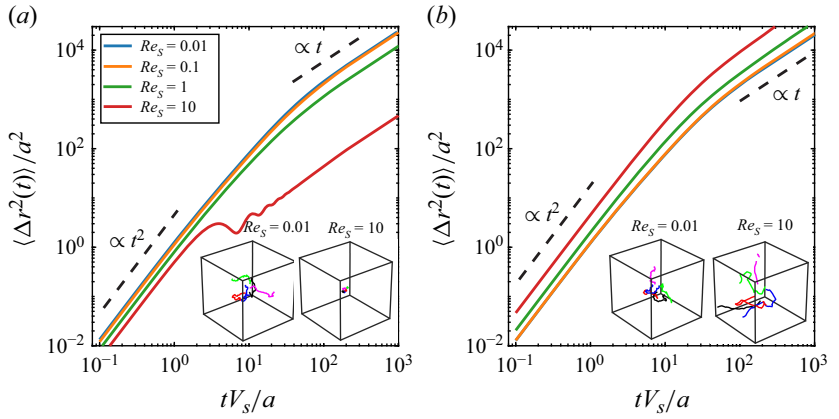


Figure 5. Mean-square displacement of (*a*) pullers and (*b*) pushers with $\phi = 0.05$ at various Reynolds numbers. Here $\tau_s = a/V_s$ is the swimming time scale. The insets show a few sample trajectories at $Re_S = 0.01$ and 10.0, respectively.

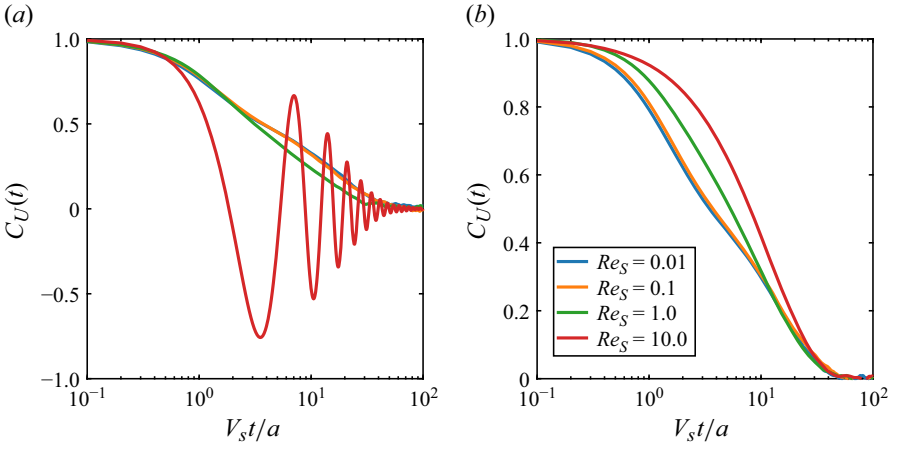


Figure 6. Velocity autocorrelation $C_U(t)$ of (*a*) pullers ($\beta = 5$) and (*b*) pushers ($\beta = -5$) at $\phi = 0.05$ over a range of swimming Reynolds numbers.

an external torque (Sandoval 2013) or shear flow (Ishikawa 2012) and bubbles rising in quiescent water (Huang *et al.* 2025). However, the underlying physical mechanisms differ substantially. In those studies, the oscillations originate from forced rotations or wake instabilities, respectively, whereas in the present case they arise from pairwise interactions.

To gain further insight into the origin of the contrasting behaviours observed for pullers and pushers, we examine the velocity autocorrelation function, which characterises the temporal persistence of swimmer motion. The normalised velocity autocorrelation function is defined as

$$C_U(t) = \frac{\langle \boldsymbol{U}(\tau) \cdot \boldsymbol{U}(\tau + t) \rangle}{\langle \boldsymbol{U}^2(\tau) \rangle}. \tag{4.3}$$

Figure 6 presents $C_U(t)$ of swimmers under different Re_S. When fluid inertia becomes non-negligible, the fore–aft antisymmetric vorticity becomes unstable, leading to a qualitative modification of hydrodynamic interactions. Consequently, near-field

https://doi.org/10.1017/jfm.2026.12141 Published online by Cambridge University Press

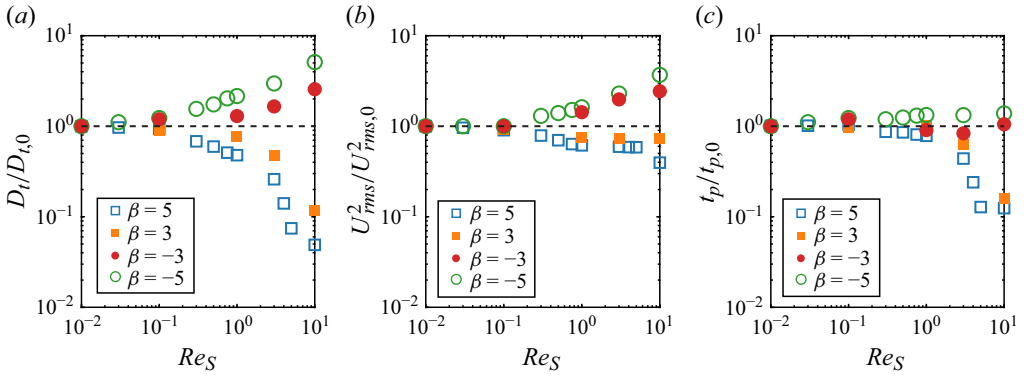


Figure 7. (*a*) Diffusion coefficient, (*b*) mean-square swimmer speed and (*c*) decorrelation time as functions of the swimming Reynolds number for different values of β at $\phi = 0.05$. All quantities are normalised by their corresponding values when $Re_S = 0.01$, i.e. $D_{t,0}$.

encounters induce stronger angular deflections, thereby accelerating the decay of velocity autocorrelation. This interpretation is consistent with previous studies on pairwise interactions (Li *et al.* 2016), which showed that pullers exhibit increasingly larger scattering angles with increasing Reynolds number. As a result, $C_U(t)$ exhibits a markedly faster decay with increasing Re_S as shown in figure 6(*a*). Notably, at $Re_S = 10$, $C_U(t)$ displays a pronounced damped oscillation around zero, which gives rise to an oscillating MSD in the intermediate-time regime in figure 5(*a*). Unlike pullers, figure 6(*b*) shows that $C_U(t)$ for pushers decays more slowly as Re_S increases. This trend can be understood from the inertia-modified wake dynamics of pushers. As the Reynolds number increases, the pusher generates a more coherent and stable wake structure, characterised by increased wake velocity and a reduced wake width (Li *et al.* 2016). Unlike pullers, whose wake tends to destabilise under inertia, pushers maintain a long-lived vorticity wake and do not exhibit immediate wake separation or a standing eddy even at moderate Re_S (Chisholm *et al.* 2016). This persistent wake stabilises pusher's orientation and thereby slowing the decay of velocity correlations.

We extract the diffusion coefficient D_t at $\phi = 0.05$ from the long-time MSDs shown in figure 7(*a*). Clearly, the results confirm that D_t decreases with Re_S for pullers, whereas it increases with Re_S for pushers. The diffusion coefficient for pullers at $Re_S = 10$ is more than an order of magnitude smaller than its value in the low-Re limit, whereas for pushers it increases several times over the same range. The figure further illustrates the effect of β on the diffusion coefficient, revealing that the sensitivity of Re_S on D_t becomes stronger as $|\beta|$ increases. The diffusion coefficient D_t can be expressed in terms of the velocity autocorrelation function through the Green–Kubo relation

$$D_t = \frac{1}{3}\int_0^\infty \langle \boldsymbol{U}(\tau)\cdot\boldsymbol{U}(\tau+t)\rangle \,\mathrm{d}t. \tag{4.4}$$

Then we have $D_t = U^2_{rms}t_p$, where $U^2_{rms} = \langle \boldsymbol{U}^2(\tau)\rangle/3$ is the mean-square speed of swimmers and $t_p = \int_0^\infty C_U(t)\,\mathrm{d}t$ is a time scale of the velocity decorrelation. Figure 7(*b*,*c*) shows U^2_{rms} and t_p of swimmers at $\phi = 0.05$, normalised by their corresponding values when $Re_S = 0.01$. For pullers, both U^2_{rms} and t_p decrease with increasing Re_S, whereas for pushers, both U^2_{rms} and t_p increase with Re_S. Consequently, fluid inertia reduces the swimming speed and accelerates the velocity decorrelation of pullers, whereas it has the

https://doi.org/10.1017/jfm.2026.12141 Published online by Cambridge University Press

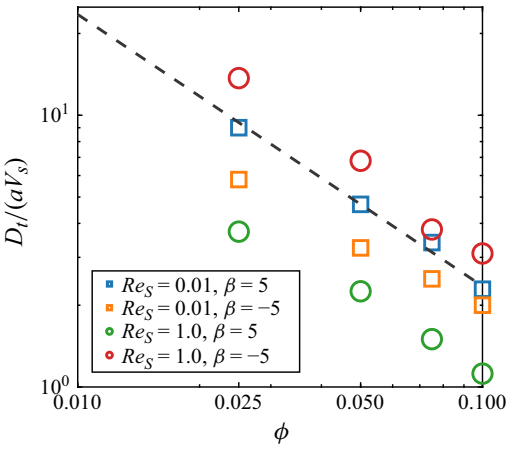


Figure 8. Correlation between D_t and ϕ at different Re_S and β. The dashed line $D_t/(aV_s) = 0.24\phi^{-1}$ (Ishikawa & Pedley 2007*a*) for $\beta = 5$ is drawn to guide the eye.

opposite effect on pushers, enhancing their swimming speed and prolonging the velocity correlation.

4.2. *Scaling of diffusion coefficient*

Dimensionally, D_t has units of $\mathrm{m}^2/\mathrm{s}^{-1}$, and so can be expressed as $U_c^2 T_c$, with U_c and T_c being the velocity and time scales. In semi-dilute suspensions of squirmers without inertia, it has been reported that D_t scales inversely with the volume fraction, i.e. $D_t \sim \phi^{-1}$ (Ishikawa & Pedley 2007*a*). We first revisit the scaling argument. In a semi-dilute suspension, the diffusive behaviour of squirmers is primarily governed by short-range two-body hydrodynamic interactions that induce significant particle reorientation. This motivates a random-walk model, yielding, for example, $D_t \sim U_{sol}^2 t_{mfp}/(1 - \langle\cos\Delta\theta\rangle)$ (Berg 1993), where U_{sol} is the swimming speed of an isolated swimmer in the absence of interactions, t_{mfp} is the effective time duration between successive collisions and $\Delta\theta$ represents the angular deflection between successive collisions. The time scale t_{mfp} can be scaled using a simple kinetic-theory argument. A swimmer sweeps out a volume $V_{swept} \sim \pi a^2 U_{sol} t_{mfp}$ in time t_{mfp}, and the number of particles within this volume is $N \sim 3\phi U_{sol} t_{mfp}/(4a)$. Requiring that $N \sim 1$ gives $t_{mfp} \sim (a/U_{sol})\phi^{-1}$. As U_{sol} and $\langle\cos\Delta\theta\rangle$ are independent on ϕ, the random-walk model results in

$$D_t \sim a U_{sol} \phi^{-1}. \tag{4.5}$$

It is important to note that the motion of non-Brownian swimmers is intrinsically deterministic. However, repeated reorientations progressively erase their orientational memory, such that the random-walk framework provides an effective description of their diffusive behaviour. In the present study, we examine whether this scaling law remains valid when finite fluid inertia is included. To this end, we plot the diffusion coefficient D_t as a function of ϕ for $Re_S = 0.01$ and 1 on a log–log scale in figure 8. The dashed line, representing the scaling $D_t/(aV_s) = 0.24\phi^{-1}$ for pullers ($\beta = 5$) in the zero-Re limit proposed by Ishikawa & Pedley (2007*a*), is included for reference. The numerical data for $Re_S = 0.01$ and $\beta = 5$ closely follow the reference line, while the results for $Re_S = 1$ continue to exhibit the inverse scaling of D_t with ϕ. Our results demonstrate that, although fluid inertia significantly modifies the diffusion coefficient, it does not alter the underlying ϕ^{-1} scaling in the presence of weak fluid inertia.

https://doi.org/10.1017/jfm.2026.12141 Published online by Cambridge University Press

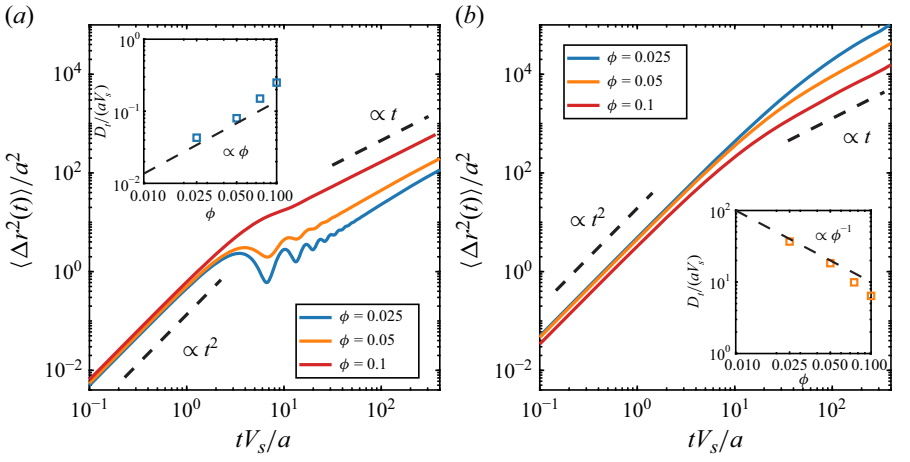


Figure 9. Effect of volume fraction ϕ on the MSDs of (a) pullers and (b) pushers in the presence of non-negligible inertial effects ($\beta = \pm 5$, $Re_S = 10$). The insets show the corresponding long-time diffusion coefficient as a function of ϕ.

However, such scaling is expected to break down at higher Re_S. Figure 9 shows the MSD of swimmers ($\beta \pm 5$, $Re_S = 10$) with ϕ ranges from 0.025 to 0.1. The MSD of pushers decreases as ϕ is increased as expected, whereas it increases as ϕ is increased for pullers. In the insets, we plot the corresponding long-time diffusion coefficient as a function of ϕ, confirming these opposite trends. This difference in behaviour stems from the qualitative differences in the two-body interactions between pullers and pushers. In the case of pushers, the two swimmers immediately separate and move in different directions upon collision. In contrast, pullers tend to move together as a stable pair without separating, as shown in figure 3(c). This stable paired motion is disrupted by collisions with a third swimmer, causing the swimmers to scatter in different directions. Consequently, as the volume fraction increases, pairwise entrapment is weakened, leading to enhanced swimmer transport. These results indicate that the introduction of inertia qualitatively alters the diffusion characteristics of pullers and pushers.

In addition, we note that the transition between these two regimes for pullers is non-trivial. For intermediate Reynolds numbers ($1 < Re_S < 10$), pairwise scattering and pairwise entrapment are both active, and their relative importance depends on both Re_S and ϕ. Consequently, no simple universal dependence of D_t on ϕ is expected in this regime. A systematic investigation of this Reynolds-number-dependent transition requires extensive simulations over a broad range of Reynolds numbers and volume fractions, and is therefore left for future work.

5. A suspension of settling swimmers

5.1. *Settling dynamics in the weak-to-moderate inertia regime*

When swimmers are denser than the surrounding fluid, they experience vertical migration. We first focus on the weak-to-moderate inertia regime ($Re_S \leqslant 1$), which is representative of most micro- and meso-scale systems. As is shown in the following, even such modest fluid inertia, when coupled with sedimentation, is sufficient to fundamentally alter the collective migration and diffusion. The influence of stronger fluid inertia ($Re_S = 10$) is examined separately in § 5.4.

https://doi.org/10.1017/jfm.2026.12141 Published online by Cambridge University Press

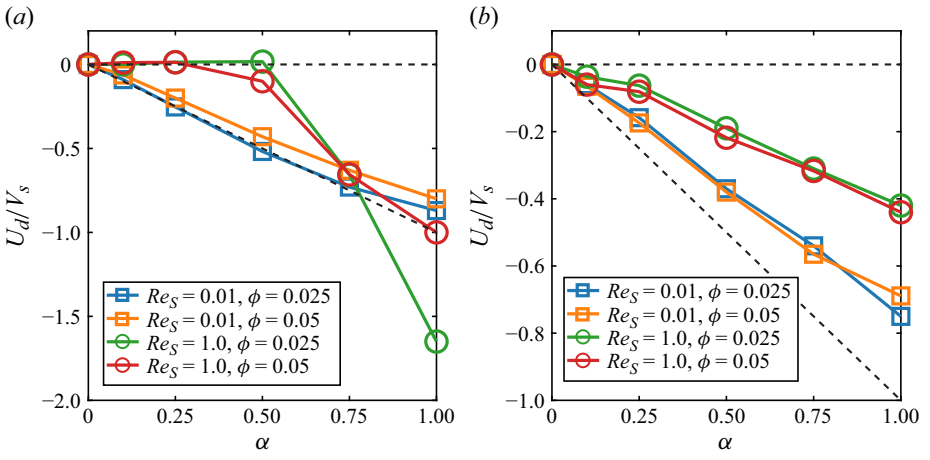


Figure 10. Vertical drift velocity of settling swimmers as a function of the settling coefficient: (*a*) $\beta = 5$ and (*b*) $\beta = -5$. The inclined dashed lines represent $U_d = -V_g$.

The vertical drift velocity is defined as

$$U_d = \lim_{t\to\infty} \frac{\langle x(\tau + t) - x(\tau)\rangle}{t}. \tag{5.1}$$

Figure 10 presents U_d as a function of settling coefficient α for $\beta = \pm 5$. The inclined dashed lines represent $U_d = -V_g$, corresponding to a simple superposition of isotropic swimming and directional sedimentation. At low Re_S, both pullers and pushers settle downwards under gravity, with settling speeds slightly smaller than the Stokes settling velocity V_s due to the hindered effect. Contrary to the common results at low Reynolds numbers, as shown in figure 10(*a*), at $Re_S = 1$ the pullers exhibit almost no net vertical migration ($U_d \simeq 0$) at low values of $\alpha \leqslant 0.5$, indicating that settling pullers are, on average, able to counteract gravitational settling in the finite-inertia regime. However, as α further increases, the downwards drift velocity increases markedly, and at $\alpha = 1$ the settling speed far exceeds that observed in the $Re_S = 0.01$ cases. This observation is clearly anomalous, as fluid inertia typically enhances hydrodynamic drag and therefore decreases the settling velocity. Pushers, on the other hand, display a more conventional behaviour. As shown in figure 10(*b*), at $Re_S = 1$ the increased hydrodynamic drag reduces their settling speed relative to the low-Re_S cases.

Beyond their vertical drift velocity, settling swimmers exhibit long-time diffusive behaviours. We discuss separately the diffusion coefficients parallel ($D_t^{\parallel}$) and perpendicular ($D_t^{\perp}$) to the gravity direction, which are computed as

$$D_t^{\parallel} = \lim_{t\to\infty} \frac{\langle \Delta r_{\parallel}^2(t)\rangle}{2t}, \quad D_t^{\perp} = \lim_{t\to\infty} \frac{\langle \Delta r_{\perp}^2(t)\rangle}{4t}. \tag{5.2}$$

Here, $\Delta r_{\parallel}^2(t) = [\hat{x}(\tau + t) - \hat{x}(\tau)]^2$, where $\hat{x}(t) = x - \int U_d \, \mathrm{d}t$ denotes the MSD in the vertical direction relative to the mean vertical displacement. Meanwhile, $\Delta r_{\perp}^2(t) = \langle [y(\tau + t) - y(\tau)]^2 + [z(\tau + t) - z(\tau)]^2 \rangle$ represents the horizontal MSD.

The results for the diffusion coefficients are shown in figure 11. At low Re_S, both the vertical and horizontal diffusion coefficients vary little with the settling coefficient, indicating that sedimentation has only a weak influence on the diffusive dynamics in the low-Re_S regime. At $Re_S = 1$, however, both $D_t^{\parallel}$ and $D_t^{\perp}$ deviate from the neutrally buoyant

https://doi.org/10.1017/jfm.2026.12141 Published online by Cambridge University Press

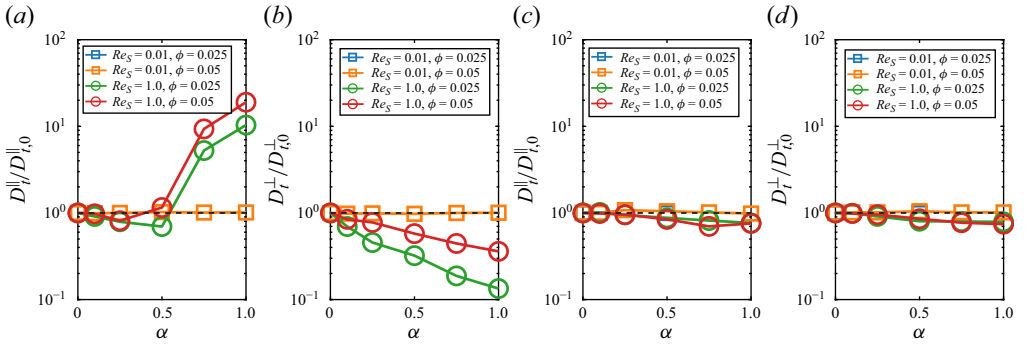


Figure 11. Relative diffusion coefficients as a function of the settling coefficient for (*a*,*b*) pullers ($\beta = 5$) and (*c*,*d*) pushers ($\beta = -5$): (*a*,*c*) $D_t^{\parallel}/D_{t,0}^{\parallel}$ and (*b*,*d*) $D_t^{\perp}/D_{t,0}^{\perp}$. Here $D_{t,0}^{\parallel}$ and $D_{t,0}^{\perp}$ represent corresponding values at $\alpha = 0$.

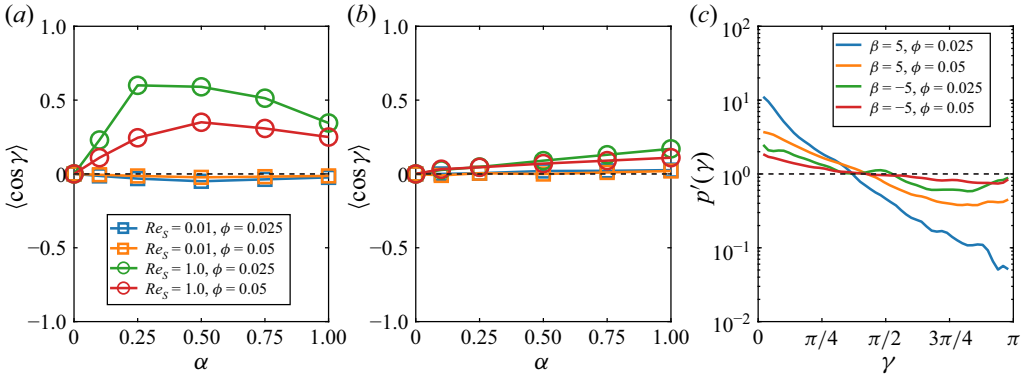


Figure 12. Dependence of the preferential orientation of swimmers on the settling coefficient. Mean orientation angle for (*a*) $\beta = 5$ and (*b*) $\beta = -5$. (*c*) Normalised angular probability density function of the orientation for inertial swimmers at $Re_S = 1$ and $\alpha = 0.5$.

cases. For pushers, both the vertical and horizontal diffusion coefficients decrease as α increases. Pullers, however, exhibit a markedly different behaviour: the vertical diffusion coefficient increases significantly for $\alpha > 0.5$, while the horizontal diffusion coefficient decreases rapidly with increasing α. In particular, $D_t^{\parallel}$ becomes more than one order of magnitude larger than that of the neutrally buoyant case for $\alpha \geqslant 0.75$. This result reveals an extreme anisotropy in the swimmer diffusion for settling pullers with finite fluid inertia.

Our observations indicate that sedimentation plays a key role in swimmer transport in the finite-inertia regime, particularly for pullers. The origin of these behaviours is examined in the following subsections.

5.2. *Preferential orientation*

To gain insight into the mechanisms underlying the observed transport behaviour, we first examine the preferential orientation of swimmers in the presence of gravity. We define γ as the angle between the orientation vector $\boldsymbol{p}$ and the positive x-axis (see figure 1*b*). Figure 12(*a*) shows the dependence of the mean orientation of pullers, quantified by $\langle \cos\gamma \rangle$, on the settling coefficient α. At low Re_S, no clear preferential orientation is observed. At $Re_S = 1$, however, pullers exhibit a positive $\langle \cos\gamma \rangle$, indicating a tendency to swim upwards against gravity. The corresponding results for pushers are shown in

https://doi.org/10.1017/jfm.2026.12141 Published online by Cambridge University Press

figure 12(*b*), where only a much weaker upwards preferential orientation is observed at $Re_S = 1$.

We introduce a normalised angular probability density function, defined as (Ishikawa & Pedley 2007*b*)

$$p'(\gamma) = \frac{2}{nV\sin(\gamma)} \iint_{\gamma=const} P(\boldsymbol{p})\,\mathrm{d}A_e\,\mathrm{d}V, \tag{5.3}$$

where $P(\boldsymbol{p})$ is the probability that there is a swimmer with an orientation vector $\boldsymbol{p}$ within the solid angle $\mathrm{d}A_e$. If one assumes isotropic orientation of swimmers, then $p'(\gamma) = 1$ for all γ. The results of $p'(\gamma)$ for swimmers ($Re_S = 1$, $\alpha = 0.5$) are shown in figure 12(*c*). Our results reveal that the $p'(\gamma)$ distribution has a peak at $\gamma = 0$ for $Re_S = 1$. Meanwhile, $p'(\gamma)$ has a larger peak for smaller ϕ due to weaker interactions among swimmers.

The gravitactic behaviour observed in figure 12 for non-bottom-heavy swimmers with sedimentation is reminiscent of that reported in bottom-heavy swimmers, which align vertically due to a gravitational torque arising from mass asymmetry (Ishikawa & Pedley 2007*a*). However, the underlying mechanisms are fundamentally different. In the finite-Re_S regime, the alignment of swimmers is governed by a hydrodynamic torque exerted on them during sedimentation, rather than from an intrinsic gravitational torque. For isolated spherical squirmers, Candelier *et al.* (2022) has demonstrated that sedimentation of squirmer generates hydrodynamic torques arising from convective fluid inertia. These torques tend to align swimmers in the opposite direction of gravity, offering a unique mechanism of gyrotaxis. In Appendix A, we perform additional simulations of individual settling swimmers, which confirm that at $Re_S = 1$, the puller experiences a substantially larger torque than the pusher.

The preferential orientation explains why puller suspensions with $Re_S = 1$ exhibit little net settlement in relatively small α, as seen in figure 10(*a*). The preferential orientation also explains the hindered diffusion of settling pushers at $Re_S = 1$ shown in figure 11(*c*,*d*). As the pushers become preferentially aligned against gravity, their orientations become much less dispersed. Consequently, neighbouring pushers tend to swim in nearly the same direction, which reduces their relative velocity and the frequency of close hydrodynamic encounters. The weakened hydrodynamic interactions lead to less-frequent reorientation and therefore suppress the long-time translational diffusion. However, preferential orientation fails to explain the anomalous vertical migration and diffusion of pullers at $Re_S = 1$ and $\alpha > 0.5$. In § 5.3, we provide a detailed analysis of the microstructure of the swimmer suspension, which offers further insights into these unusual transport phenomena.

5.3. *Inhomogeneous structures*

Sedimentation of swimmers will induce various microstructures and collective organisation, which can substantially alter the transport phenomena of swimmers. In order to quantify the microstructure of suspensions, we examine the pair correlation function $g(\boldsymbol{r}_g)$ (Kulkarni & Morris 2008), which represents the normalised probability of finding a particle within a finite-volume element centred at the relative separation vector $\boldsymbol{r}_g$,

$$g(\boldsymbol{r}_g) = \frac{P_{1|1}(\boldsymbol{r}_g \mid \boldsymbol{0})}{n}, \tag{5.4}$$

where $n = N/L^3$ is the average number density and $P_{1|1}(\boldsymbol{r}_g \mid \boldsymbol{0})$ is the conditional probability density of finding a particle at $\boldsymbol{r}_g$, given that a reference particle is located

https://doi.org/10.1017/jfm.2026.12141 Published online by Cambridge University Press

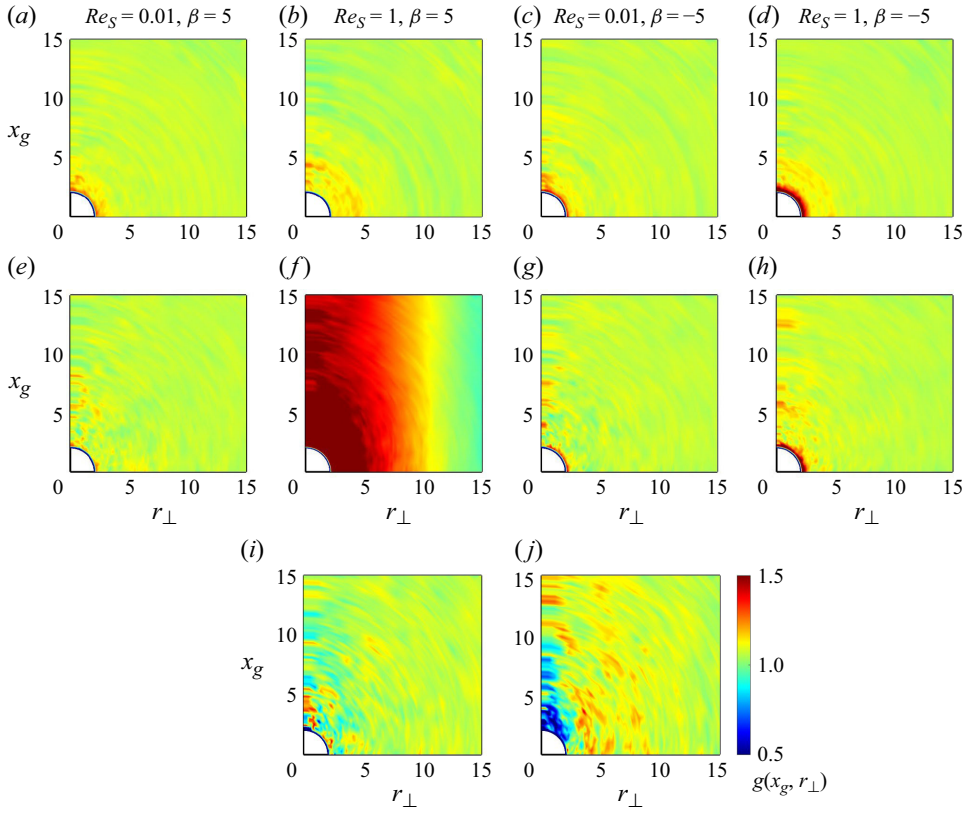


Figure 13. Pair correlation functions $g(r_\perp, x_g)$ of swimmers at volume fraction of $\phi = 0.025$: (*a–d*) $\alpha = 0$; (*e–h*) $\alpha = 1.0$. For reference, the pair correlation functions of passive suspensions are shown: (*i*) $Re_G = 0.01$ and (*j*) $Re_G = 1$.

at the origin $\mathbf{0}$. In the numerical implementation, $P_{1|1}(\boldsymbol{r}_g \mid \mathbf{0})$ is estimated by counting swimmer pairs within finite volume elements.

For suspensions in the absence of gravity, particle pairs are expected to be isotropically distributed, resulting in a radially symmetric pair correlation function. In contrast, in sedimenting suspensions, previous numerical results indicated that the settling of passive particles has anisotropic microstructures (Yin & Koch 2007; Xia *et al.* 2022, 2024, 2025*a*). Since the horizontal distribution remains approximately isotropic, the relative position vector $\boldsymbol{r}_g = (x_g, y_g, z_g)^T$ can be decomposed into vertical and horizontal components,

$$\boldsymbol{r}_g = \boldsymbol{r}_\perp + x_g \boldsymbol{e}_x, \quad \text{with} \quad \boldsymbol{r}_\perp = y_g \boldsymbol{e}_y + z_g \boldsymbol{e}_z, \quad r_\perp = \|\boldsymbol{r}_\perp\| = \sqrt{y_g^2 + z_g^2}. \tag{5.5}$$

As a result, the three-dimensional pair correlation function $g(\boldsymbol{r}_g)$ is averaged over the azimuthal direction and represented as $g(r_\perp, x_g)$. Figure 13 shows the pair correlation functions $g(r_\perp, x_g)$ for suspensions of both neutrally buoyant swimmers ($\alpha = 0$) and settling swimmers ($\alpha = 1$) for $\phi = 0.025$. Figure 13(*a–d*) confirm that the microstructure of neutrally buoyant swimmers is nearly isotropic, with a high probability of finding swimmer pairs in near contact in all directions. In contrast, a higher pair correlation is observed for settling swimmer pairs with vertical separation (figure 13*e–h*). In particular, as shown in figure 13(*f*), $g(r_\perp, x_g)$ exhibits pronounced values along the vertical direction for pullers with $Re_S = 1$, indicating a column-like structure. Such columnar clustering

https://doi.org/10.1017/jfm.2026.12141 Published online by Cambridge University Press

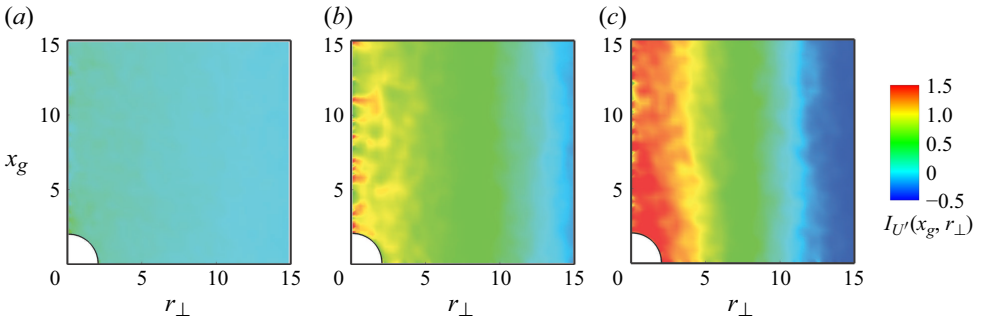


Figure 14. Velocity correlation functions $I_{U'}(r_\perp, x_g)$ of settling pullers ($\beta = 5$, $Re_S = 1.0$, $\phi = 0.025$): (a) $\alpha = 0.5$, (b) $\alpha = 0.75$ and (c) $\alpha = 1.0$.

has been previously reported in dilute passive suspensions at high settling Reynolds numbers ($Re_G \gg O(10)$), where it originates from wake-induced hydrodynamic attraction (Uhlmann & Doychev 2014; Moriche *et al.* 2023; Jiang *et al.* 2024). However, this mechanism is not applicable here, since the present regime is restricted to $Re_G \leqslant 1$, where wake effects are weak. To further isolate the underlying mechanism, we examine passive particles at $Re_G = 0.01$ and 1, respectively (figure 13*i*,*j*). In both cases, no columnar structures are observed. At $Re_G = 1$, we observe a decreased pair distribution function for pairs with vertical separation, which is consistent with previous studies (Yin & Koch 2007; Xia *et al.* 2022). Taken together, these results indicate that the observed column-like structures arise uniquely in suspensions of settling pullers, and cannot be attributed to either classical wake-induced attraction.

Pullers exhibits a much stronger tendency to reorient against gravity than pushers owing to a stronger fluid-inertial torque. Although the restoring torque originates from fluid inertia rather than bottom-heaviness, the resulting orientational dynamics are qualitatively analogous to those of gyrotactic swimmers. An upwards-oriented puller simultaneously settles under gravity, generating a disturbance flow associated with its sedimentation. Equivalently, the sedimentation-induced disturbance flow establishes a local hydrodynamic shear that tends to rotate neighbouring swimmers. Due to a balance between fluid-inertial torque and shear-induced torques, this self-generated shear favours the reorientation and gradual migration of pullers towards the descending flow region, thereby promoting vertically aligned clustering.

While the above results demonstrate the emergence of anisotropic, column-like microstructures for settling pullers in the finite-inertia regime, they do not fully capture the coherence of the swimmer motion. To quantify the coherent motion, we compute the following pair correlation functions for the velocity fluctuations:

$$I_{U'}\left(\boldsymbol{r}_g\right) = \left\langle U_x'\left(\boldsymbol{x}_i\right) U_x'\left(\boldsymbol{x}_j\right) \mid \boldsymbol{r}_{ij} = \boldsymbol{r}_g \right\rangle, \tag{5.6}$$

where $U_x'(\boldsymbol{x}_i) = U_x(\boldsymbol{x}_i) - \langle U_x \rangle$ is the x component of the velocity fluctuation of swimmer i. Figure 14 shows $I_{U'}(r_\perp, x_g)$ for settling pullers at $Re_S = 1$ with increasing settling. Figure 14(*a*) indicates that the velocity fluctuations are nearly decorrelated at all relative positions between swimmer pairs at $\alpha = 0.5$. As α increases, a pronounced positive correlation emerges at small horizontal separations, while a negative correlation is observed at separations larger than $10a$ (figure 14*c*). These results indicate that stronger sedimentation and column-like structure will induce large-scale, vertically coherent flows in puller suspensions with finite inertia. The velocity correlations further demonstrate

https://doi.org/10.1017/jfm.2026.12141 Published online by Cambridge University Press

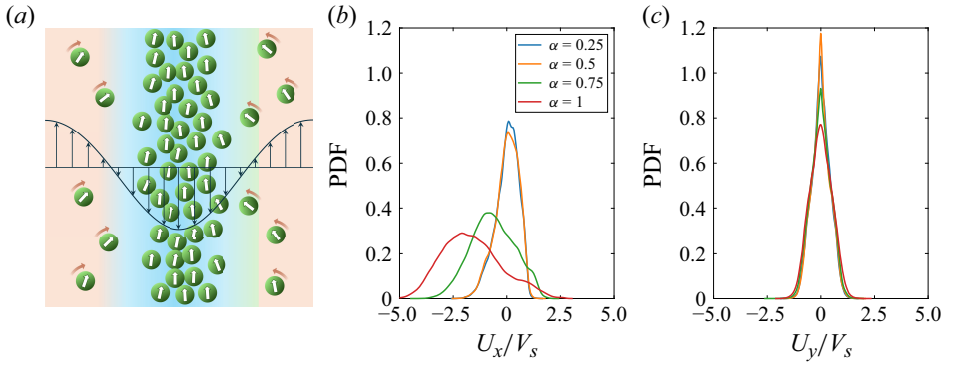


Figure 15. (*a*) Illustration for the columnar structure and coherent flow in settling puller suspensions. The background colour represents the streamwise fluid velocity fluctuation, where blue corresponds to downwelling and red corresponds to upwelling. Probability density functions of instantaneous swimmer ($\beta = 5$, $Re_S = 1.0$, $\phi = 0.025$) velocities in the (*b*) x and (*c*) y directions for different values of α.

that the columnar microstructures are accompanied by coherent downwelling motions extending over many swimmer diameters, indicating that the swimmer accumulation is dynamically coupled with the surrounding disturbance flow. As shown in figure 15(*a*), such a downwelling flow generates vorticity that reorients the surrounding swimmers towards the direction of the downwelling flow. The increased local concentration within the columns further strengthens the descending disturbance flow. This mutual reinforcement establishes a positive feedback between swimmer accumulation and coherent downwelling, thereby sustaining the columnar organisation. Consequently, pullers preferentially reside within coherent downwelling regions than in a spatially homogeneous suspension, resulting in a significantly enhanced mean settling velocity. Taken together, the resulting collective dynamics can be interpreted within the framework of gyrotactic focusing (Kessler 1985, 1986; Pedley & Kessler 1992; Croze *et al.* 2017; Rühle *et al.* 2022; Ishikawa *et al.* 2025*a*), in which the competition between fluid shear and a restoring torque drives the preferential accumulation of negatively buoyant swimmers. Although the restoring torque in the present system originates from fluid inertia rather than bottom-heaviness, the resulting collective organisation is qualitatively analogous to classical gyrotactic focusing.

The same coherent organisation also accounts for the anisotropic diffusion. As shown in figure 15, the coexistence of coherent downwelling within the columns and compensating upwards flow in the surrounding dilute regions broadens the distribution of streamwise swimmer velocities (figure 15*b*), thereby increasing the vertical velocity variance. Conversely, because swimmers remain laterally confined within columns due to gyrotactic focusing, transverse relative motion is suppressed, leading to a reduced horizontal velocity variance (figure 15*c*). Consequently, the diffusion becomes increasingly anisotropic with increasing settling strength, characterised by enhanced transport in the vertical direction and reduced transport in the horizontal directions. The coherent collective dynamics associated with this gyrotactic-focusing-like state therefore provide a unified explanation for the enhanced settling velocity and strongly anisotropic diffusion observed in finite-inertia puller suspensions.

We note that the column-like structures and large-scale disturbance flows are constrained by the finite computational domain with periodic boundary conditions. Consequently, when inhomogeneous structures emerge (see Appendix B), the quantitative values of the drift velocity and diffusion coefficient exhibit some dependence on the domain size.

https://doi.org/10.1017/jfm.2026.12141 Published online by Cambridge University Press

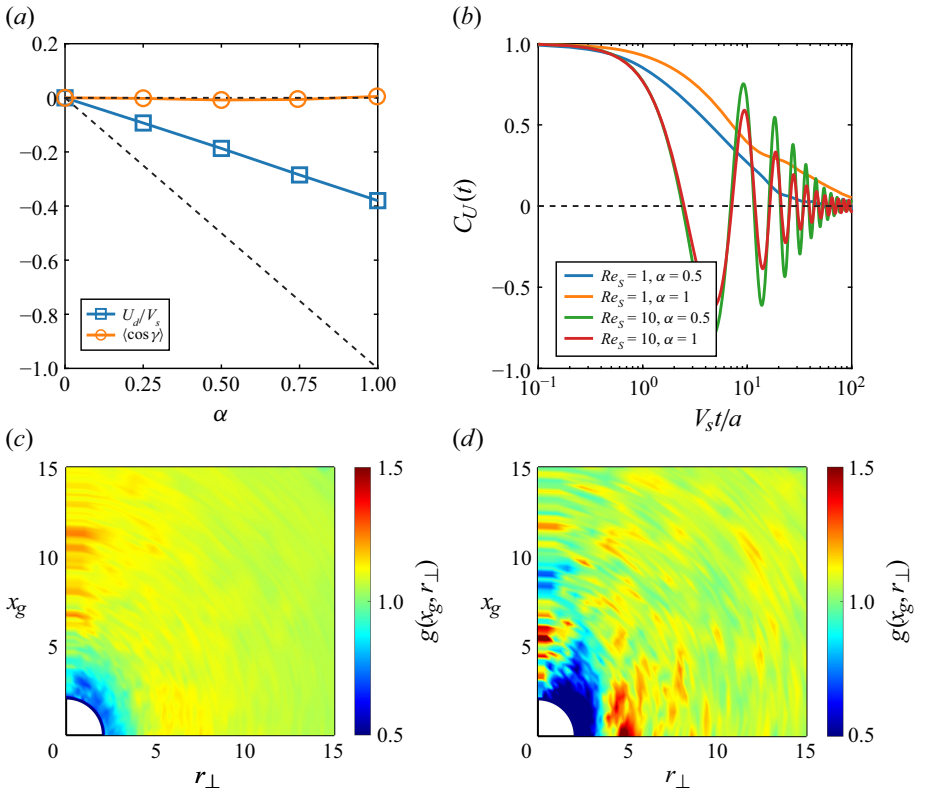


Figure 16. Dynamics of settling pullers ($\beta = 5$ and $\phi = 0.025$). (*a*) Vertical drift velocity as a function of the settling coefficient at $Re_S = 10$. (*b*) Velocity autocorrelation. (*c*) Pair correlation function with $\alpha = 1$. For reference, (*d*) shows the pair correlation function of passive suspension with $Re_G = 10$.

Nevertheless, the qualitative conclusions regarding the formation of microstructures, the enhanced drift, as well as the anisotropic diffusion remain unaffected.

5.4. *Settling dynamics in the high-inertia regime*

The preceding subsections demonstrated that moderate fluid inertia ($Re_S = 1$) promotes settling-induced preferential orientation and collective organisation for pullers. A natural question is whether these collective states are further enhanced at higher Reynolds numbers, where isolated pullers experience an even stronger inertial torque. To address this issue, we additionally consider settling pullers ($\beta = 5$ and $\phi = 0.025$) at $Re_S = 10$. In figure 16(*a*) we plot the vertical drift velocity and the mean orientation angle as a function of settling coefficient. Surprisingly, in contrast to the moderate-inertia regime, the suspension no longer develops any collective ordering, and the settling speed increases with increasing settling coefficient. The disappearance of preferential orientation at $Re_S = 10$ cannot be attributed to a weaker fluid-inertial aligning torque. On the contrary, isolated pullers exhibit even stronger upwards alignment at this Reynolds number. We attribute the suppression of collective migration to the persistent pairwise entrapment characteristic of pullers at $Re_S \sim O(10)$. Figure 16(*b*) compares the velocity autocorrelation function $C_U(t)$ of settling pullers at $Re_S = 1$ and 10. At $Re_S = 10$, the oscillatory velocity autocorrelation remains prominent when settling is introduced, indicating that the pairwise dynamics identified in § 4 remain the dominant hydrodynamic

https://doi.org/10.1017/jfm.2026.12141 Published online by Cambridge University Press

interaction. Although the fluid-inertial torque continuously drives swimmers toward an upwards-swimming state, repeated pairwise encounters prevent this alignment from being maintained over long times. Consequently, sustained gyrotactic focusing cannot be established, leading to the disappearance of collective organisation.

Figure 16(*c*) further displays the pair correlation function of pullers with $Re_S = 10$ and $\alpha = 1$, confirming that the pronounced vertically aligned structure observed in figure 13(*f*) disappear at higher Reynolds numbers. For comparison, we also include the pair correlation function of passive particles at $Re_G = 10$ in figure 16(*d*). In both cases, the probability of finding particle pairs in near contact is reduced, which suggests that the pairwise interactions destroy the vertical structure, so that, after averaging, the resulting distribution resembles that of passive particles settling under gravity.

Consequently, the collective migration identified at moderate Reynolds numbers no longer develops in the high-inertia regime. The non-trivial phenomenon highlights the importance of investigating the Reynolds-number dependence of collective migration of swimmers under gravity. We plan to explore the state transition in future work.

6. Concluding remarks

In this paper we have investigated the diffusion, migration and microstructure of swimmers in a semi-dilute suspension, accounting for both fluid inertia and gravitational settling. Direct numerical simulations have been performed to resolve the dynamics of both neutrally buoyant and settling squirmers in a triply periodic cubic domain.

For neutrally buoyant squirmers, increasing fluid inertia leads to qualitatively different diffusion responses, with suppression observed for pullers and enhancement for pushers. This contrasting behaviour originates from the distinct inertial responses of pullers and pushers. Fluid inertia suppresses the swimming speed of pullers and causes their velocity to decorrelate significantly faster, thereby reducing their diffusion, whereas pushers display the opposite tendency. Scaling analysis further demonstrates that the diffusion coefficient is inversely proportional to the swimmer volume fraction in the weakly inertial regime ($Re_S \leqslant 1$), while this scaling breaks down at higher Reynolds numbers. In particular, for pullers, persistent pairwise entrapment becomes less stable as the volume fraction increased, leading to enhanced diffusion.

For settling squirmers, sedimentation significantly modifies transport at moderate-inertia regime. In this regime, fluid-inertial torques induce a systematic reorientation of swimmers against gravity. This preferential alignment alters both the collective organisation and the resulting transport properties of swimmers. In particular, the reorientation tends to suppress spreading in pushers by reducing the effectiveness of the inter-swimmer interactions. On the other hand, analogous to the classical gyrotactic focusing of bottom-heavy swimmers, this preferential alignment promotes the formation of coherent vertical structures in puller suspensions, causing swimmers to preferentially accumulate in downdraughts and thereby enhancing vertical velocity fluctuations. As a consequence, both the drift velocity and the vertical diffusion of pullers are markedly enhanced. We further demonstrate that this collective migration is confined to the moderate-inertia regime. At higher Reynolds numbers ($Re_S = 10$), the emergence of pairwise entrapment suppresses the upwards swimming tendency and the formation of coherent columns.

This study represents a first step towards understanding the modified transport phenomena of swimmers with non-negligible fluid inertia and sedimentation. The non-trivial roles of fluid inertia and gravitational settling highlight the need for theoretical models that explicitly incorporate inertial and sedimentation-induced effects, as these

https://doi.org/10.1017/jfm.2026.12141 Published online by Cambridge University Press

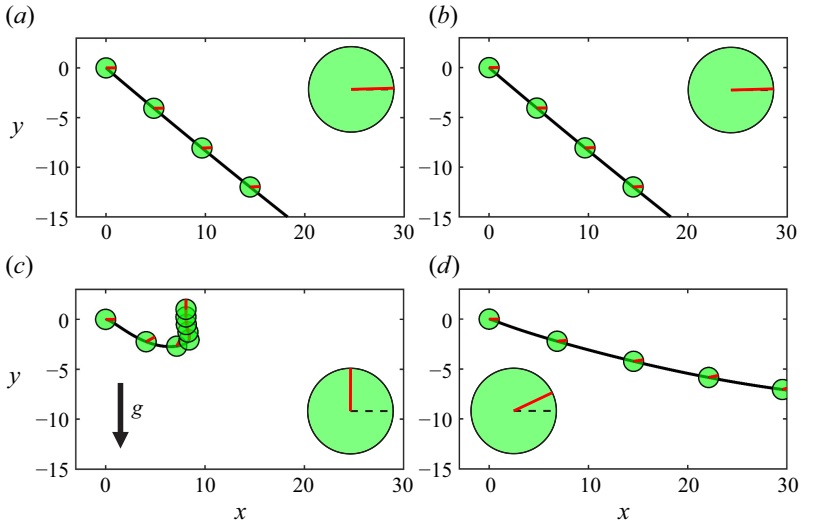


Figure 17. Trajectories and orientations of isolated swimmers at $\alpha = 1$: (*a*) $\beta = 5$, $Re_S = 0.01$; (*b*) $\beta = -5$, $Re_S = 0.01$; (*c*) $\beta = 5$, $Re_S = 1.0$; (*d*) $\beta = -5$, $Re_S = 1.0$. The insets show the corresponding finial orientations of the swimmer.

mechanisms can fundamentally reshape microstructure and large-scale transport. Future research could investigate the transport phenomena of swimmers in more complex environments, such as confined geometries, shear flows or background turbulence. Another intriguing avenue is to consider swimmers with bottom-heavy configurations or non-spherical shapes, where gravitational torques and geometric anisotropy may produce richer transport behaviours.

Funding. The work was supported by the National Natural Science Foundation of China (grant numbers 12302340, 12132015 and 12332015), JSPS KAKENHI (grants numbers 24KF0097, 21H04999, 21H05308 and 26H02595) and JST CREST (grant number JPMJCR25Q1).

Declaration of interests. The authors report no conflict of interest.

Appendix A. Dynamics of individual settling swimmers

Looking at the dynamics of individual swimmers can provide insights into the preferential orientation of swimmers shown in figure 12. Candelier *et al.* (2022) reported that spherical squirmers experience a hydrodynamic torque when settling in a quiescent fluid. This torque arises from the rotational asymmetry of the disturbance flow generated by the combined effects of swimming and sedimentation in the inertial regime. For this reason, this contribution is commonly referred to as a *fluid-inertial torque*.

To further clarify the physical mechanism, we first analyse the trajectories of an isolated swimmer. We place a single settling swimmer in a fluid, initially oriented along the horizontal direction. Figure 17 presents the corresponding trajectories and orientations for different combinations of (β, Re_S) at $\alpha = 1$. The trajectories reveal that, for pullers, increasing the Reynolds number significantly enhances the tendency for reorientation (figure 17*a*,*c*). In comparison, pushers display a much weaker sensitivity to inertia, with only minor changes in orientation observed in both values of Re_S (figure 17*b*,*d*). These observations are consistent with the trends reported in figure 12.

A deeper understanding of the fluid-inertia torque requires evaluating the hydrodynamic torque on swimmers directly. Assume that a spherical squirmer swims with swimming

https://doi.org/10.1017/jfm.2026.12141 Published online by Cambridge University Press

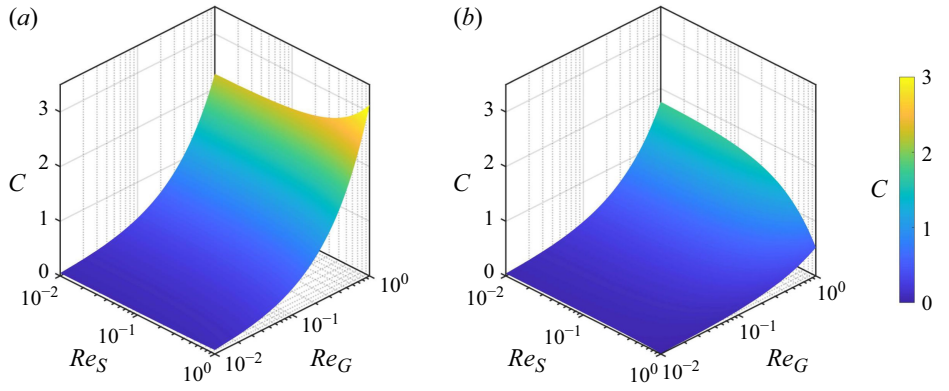


Figure 18. Normalised fluid-inertial torque, $C = T_{max}/((4/3)\pi a^3 \rho_f V_s V_g)$, on a swimmer as a function of Re_S and Re_G, obtained by a fitting process: (*a*) puller ($\beta = 5$) and (*b*) pusher ($\beta = -5$).

speed $\boldsymbol{v}_s$ while settling under gravity with velocity $\boldsymbol{v}_g$. The resulting fluid-inertial torque can be expressed as (Candelier *et al.* 2022)

$$\boldsymbol{T}_h = C\frac{4}{3}\pi a^3 \rho_f \left(\boldsymbol{v}_s \wedge \boldsymbol{v}_g\right), \tag{A1}$$

where C is a dimensionless coefficient (i.e. normalised torque) that depends on both the Reynolds numbers and the active stress β. This expression reveals that the torque scales with the product of the swimming and settling velocities. However, their roles are not symmetric. We aim to elucidate how the settling and swimming affect the fluid-inertial torque by evaluating the coefficient C. To this end, we conduct 18 simulations, considering all combinations of Re_S and Re_G with values of 0.01, 0.1 and 1, for both puller and pusher cases. Following the work of Candelier *et al.* (2022), we froze the orientation of the swimmer along the horizontal direction, but allow it to translate. In this configuration, the swimmer experiences the largest torque T_{max}. We measured T_{max} after the quasi-steady state reached. Then the coefficient can be computed by $C = T_{max}/((4/3)\pi a^3 \rho_f V_s V_g)$. Figure 18 shows the best-fit C as functions of Re_S and Re_G, which exhibits a strong dependence on Re_G, with a comparatively weaker dependence on Re_S. In the Stokesian sedimentation ($Re_G \to 0$), the torque vanishes, consistent with the Stokes approximation in which no net hydrodynamic torque arises. Comparing the coefficients for $\beta = \pm 5$ at $Re_S = Re_G = 1$ shows that the puller experiences a substantially larger torque than the pusher, in agreement with the trajectories displayed in figure 17(*c*,*d*).

Appendix B. System size dependence

To model a suspension of infinite extent, periodic boundary conditions are employed in the present study. We investigate the effect of domain size in cases of both neutrally buoyant and settling pullers ($\beta = 5$) in the finite-inertia regime ($Re_S = 1$) by employing a larger domain size of $L = 64a$. In figure 19(*a*), we compare the MSD curves of neutrally buoyant pullers at $\phi = 0.05$. The results indicate that the diffusion is weakly dependent on L, since the transport of swimmers is governed primarily by short-range hydrodynamic interactions. In contrast, figure 19(*b*) presents the MSD of settling pullers ($\alpha = 1$) at $\phi = 0.025$. Here, a noticeable increase in MSD is observed when the domain size is enlarged. The inset in figure 19(*b*) displays the corresponding particle velocity correlation function along the horizontal axis, indicating that the size of the microstructure increases

https://doi.org/10.1017/jfm.2026.12141 Published online by Cambridge University Press

Domain size	Neutrally buoyant ($\phi = 0.05, \alpha = 0$) $D_t/(aV_s)$	Settling U_d/V_s	($\phi = 0.025, \alpha = 1$) $D_t^{\parallel}/(aV_s)$
$L = 32a$	2.25	−1.65	38.6
$L = 64a$	2.32	−2.43	81.2

Table 2. Effects of domain size L on the long-time transport properties of pullers ($\beta = 5$, $Re_S = 1$).

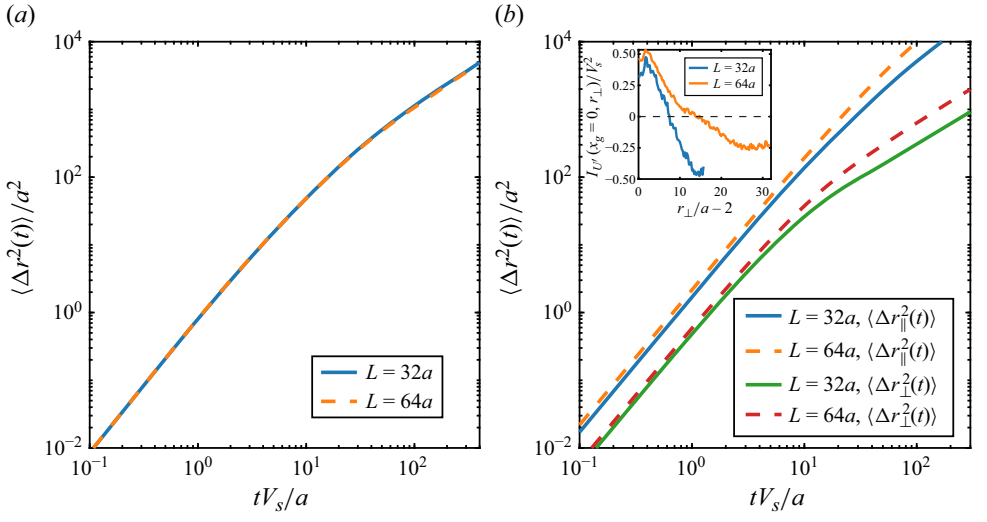


Figure 19. Mean-square displacements of (*a*) neutrally buoyant pullers ($\phi = 0.05$) and (*b*) settling pullers ($\phi = 0.025$, $\alpha = 1$) at $Re_S = 1$. The inset in (*b*) shows the vertical velocity correlation functions of swimmers along the horizontal axis.

as the domain size increases. The results highlight that the large-scale structures in puller suspension with finite inertia and sedimentation are constrained by the finite computational domain. This suggests the size of computational domain can have non-negligible effects on the swimmer dynamics.

In table 2 we list the long-time diffusive and migration properties for both domain sizes. The results confirm that the system size of $L = 32a$ is large enough for neutrally buoyant cases. However, for settling pullers at finite inertia, the magnitudes of both the drift velocity and vertical diffusion coefficient increase markedly with increasing L, reflecting the sensitivity of microstructures to the spatial extent. Such system-size dependence is not unexpected, since emergent collective structures may extend over length scales comparable to the computational domain and therefore cannot be entirely eliminated in finite domain with periodic boundaries. Considering that enlarging the domain size substantially increases the computational cost, the choice of $L = 32a$ represents a reasonable compromise between physical fidelity and computational feasibility. It reliably captures the qualitative behaviour and supports the main physical conclusions.

https://doi.org/10.1017/jfm.2026.12141 Published online by Cambridge University Press

References

Aranson, I.S. 2022 Bacterial active matter. *Rep. Prog. Phys.* **85** (7), 076601.

Ardekani, A.M., Doostmohammadi, A. & Desai, N. 2017 Transport of particles, drops, and small organisms in density stratified fluids. *Phys. Rev. Fluids* **2** (10), 100503.

Barriuso, G., Miguel, C., Serna, H., Pagonabarraga, I. & Valeriani, C. 2025 Sedimentation and structure of squirmer suspensions under gravity. *Soft Matt.* **21** (11), 2010–2025.

Bees, M.A. 2020 Advances in bioconvection. *Annu. Rev. Fluid Mech.* **52** (1), 449–476.

Berg, H.C. 1993 *Random Walks in Biology*. Princeton University Press.

Blake, J.R. 1971 A spherical envelope approach to ciliary propulsion. *J. Fluid Mech.* **46** (1), 199–208.

Candelier, F., Qiu, J., Zhao, L., Voth, G. & Mehlig, B. 2022 Inertial torque on a squirmer. *J. Fluid Mech.* **953**, R1.

Chamolly, A. & Ishikawa, T. 2026 Self-organised structures in mixed active–passive suspensions due to hydrodynamic interactions. *J. Fluid Mech.* **1030**, A22.

Chisholm, N.G., Legendre, D., Lauga, E. & Khair, A.S. 2016 A squirmer across Reynolds numbers. *J. Fluid Mech.* **796**, 233–256.

Croze, O.A., Bearon, R.N. & Bees, M.A. 2017 Gyrotactic swimmer dispersion in pipe flow: testing the theory. *J. Fluid Mech.* **816**, 481–506.

Cunha, F.R., Abade, G.C., Sousa, A.J. & Hinch, E.J. 2002 Modeling and direct simulation of velocity fluctuations and particle-velocity correlations in sedimentation. *J. Fluids Engng* **124** (4), 957–968.

De Lillo, F., Cencini, M., Durham, W.M., Barry, M., Stocker, R., Climent, E. & Boffetta, G. 2014 Turbulent fluid acceleration generates clusters of gyrotactic microorganisms. *Phys. Rev. Lett.* **112**, 044502.

Derr, N.J., Dombrowski, T., Rycroft, C.H. & Klotsa, D. 2022 Reciprocal swimming at intermediate Reynolds number. *J. Fluid Mech.* **952**, A8.

Dombrowski, C., Cisneros, L., Chatkaew, S., Goldstein, R.E. & Kessler, J.O. 2004 Self-concentration and large-scale coherence in bacterial dynamics. *Phys. Rev. Lett.* **93** (9), 098103.

Dombrowski, T., Nguyen, H. & Klotsa, D. 2022 Pairwise interactions between model swimmers at intermediate Reynolds numbers. *Phys. Rev. Fluids* **7** (7), 074401.

Drescher, K., Leptos, K.C., Tuval, I., Ishikawa, T., Pedley, T.J. & Goldstein, R.E. 2009 Dancing volvox: hydrodynamic bound states of swimming algae. *Phys. Rev. Lett.* **102** (16), 168101.

Durham, W.M., Climent, E., Barry, M., De Lillo, F., Boffetta, G., Cencini, M. & Stocker, R. 2013 Turbulence drives microscale patches of motile phytoplankton. *Nat. Commun.* **4**, 2148.

Durham, W.M., Kessler, J.O. & Stocker, R. 2009 Disruption of vertical motility by shear triggers formation of thin phytoplankton layers. *Science* **323** (5917), 1067–1070.

Evans, A.A., Ishikawa, T., Yamaguchi, T. & Lauga, E. 2011 Orientational order in concentrated suspensions of spherical microswimmers. *Phys. Fluids* **23** (11), 111702.

Fung, L. 2023 Analogy between streamers in sinking spheroids, gyrotactic plumes and chemotactic collapse. *J. Fluid Mech.* **961**, A12.

Ge, Z., Brady, J.F. & Elfring, G.J. 2025 Nonmonotonic diffusion in sheared active suspensions of squirmers. *Phys. Rev. Lett.* **135** (23), 238302.

Ge, Z. & Elfring, G.J. 2025 Hydrodynamic diffusion in apolar active suspensions of squirmers. *J. Fluid Mech.* **1003**, A17.

Hayakawa, H. & Ichiki, K. 1995 Statistical theory of sedimentation of disordered suspensions. *Phys. Rev. E* **51** (5), R3815.

Hemmersbach, R. & Häder, D.-P. 1999 Graviresponses of certain ciliates and flagellates. *FASEB J.* **13**, S69–S75.

Huang, G., Hessenkemper, H., Tan, S., Ni, R., Sommer, A., Bragg, A.D. & Ma, T. 2025 Taylor dispersion of bubble swarms rising in quiescent liquid. *J. Fluid Mech.* **1014**, R1.

Ishikawa, T. 2012 Vertical dispersion of model microorganisms in horizontal shear flow. *J. Fluid Mech.* **705**, 98–119.

Ishikawa, T. 2024 Fluid dynamics of squirmers and ciliated microorganisms. *Annu. Rev. Fluid Mech.* **56**, 119–145.

Ishikawa, T. 2025 Transport phenomena in microswimmer suspensions: migration, collective motion, diffusion and rheology. *J. Fluid Mech.* **1016**, P1.

Ishikawa, T., Brumley, D.R. & Pedley, T.J. 2025*a* Poiseuille flow of a concentrated suspension of squirmers. *J. Fluid Mech.* **1003**, A23.

Ishikawa, T., Locsei, J.T. & Pedley, T.J. 2008 Development of coherent structures in concentrated suspensions of swimming model micro-organisms. *J. Fluid Mech.* **615**, 401–431.

https://doi.org/10.1017/jfm.2026.12141 Published online by Cambridge University Press

ISHIKAWA, T. & PEDLEY, T.J. 2007*a* Diffusion of swimming model micro-organisms in a semi-dilute suspension. *J. Fluid Mech.* **588**, 437–462.
ISHIKAWA, T. & PEDLEY, T.J. 2007*b* The rheology of a semi-dilute suspension of swimming model micro-organisms. *J. Fluid Mech.* **588**, 399–435.
ISHIKAWA, T., SATO, K., OMORI, T. & YOSHIMURA, K. 2025*b* Physics of microbial taxis and behaviours in response to various physical stimuli. *Philos. Trans. R. Soc. A* **383**, 20240264.
ISHIKAWA, T., SIMMONDS, M.P. & PEDLEY, T.J. 2006 Hydrodynamic interaction of two swimming model micro-organisms. *J. Fluid Mech.* **568**, 119–160.
JEANNERET, R.ËL, PUSHKIN, D.O., KANTSLER, V. & POLIN, M. 2016 Entrainment dominates the interaction of microalgae with micron-sized objects. *Nat. Commun.* **7**, 12518.
JIANG, W. & CHEN, G. 2020 Dispersion of gyrotactic micro-organisms in pipe flows. *J. Fluid Mech.* **889**, A18.
JIANG, X., XU, C. & ZHAO, L. 2024 Prolate spheroids settling in a quiescent fluid: clustering, microstructures and collisions. *J. Fluid Mech.* **1000**, A49.
KAGE, A., OMORI, T., KIKUCHI, K. & ISHIKAWA, T. 2020 The shape effect of flagella is more important than bottom-heaviness on passive gravitactic orientation in *Chlamydomonas reinhardtii*. *J. Expl Biol.* **223**, jeb205989.
KESSLER, J.O. 1985 Hydrodynamic focusing of motile algal cells. *Nature* **313**, 218–220.
KESSLER, J.O. 1986 Individual and collective fluid dynamics of swimming cells. *J. Fluid Mech.* **173**, 191–205.
KHAIR, A.S. & CHISHOLM, N.G. 2014 Expansions at small Reynolds numbers for the locomotion of a spherical squirmer. *Phys. Fluids* **26** (1), 011902.
KIØRBOE, T., JIANG, H. & COLIN, S.P. 2010 Danger of zooplankton feeding: the fluid signal generated by ambush-feeding copepods. *Proc. R. Soc. B: Biol. Sci.* **277** (1698), 3229–3237.
KLOTSA, D. 2019 As above, so below, and also in between: mesoscale active matter in fluids. *Soft Matt.* **15** (44), 8946–8950.
KUBO, K., OMORI, T. & ISHIKAWA, T. 2025 Microstructure and deformation in suspensions of soft microswimmers. *J. Fluid Mech.* **1011**, A31.
KUHR, J.-T., BLASCHKE, J., RÜHLE, F. & STARK, H. 2017 Collective sedimentation of squirmers under gravity. *Soft Matt.* **13** (41), 7548–7555.
KULKARNI, P.M. & MORRIS, J.F. 2008 Suspension properties at finite Reynolds number from simulated shear flow. *Phys. Fluids* **20** (4), 040602.
LAUGA, E. 2020 *The Fluid Dynamics of Cell Motility*, vol. 62. Cambridge University Press.
LEPTOS, K.C., GUASTO, J.S., GOLLUB, J.P., PESCI, A.I. & GOLDSTEIN, R.E. 2009 Dynamics of enhanced tracer diffusion in suspensions of swimming eukaryotic microorganisms. *Phys. Rev. Lett.* **103** (19), 198103.
LI, G., OSTACE, A. & ARDEKANI, A.M. 2016 Hydrodynamic interaction of swimming organisms in an inertial regime. *Phys. Rev. E* **94** (5), 053104.
LI, G.-J. & ARDEKANI, A.M. 2014 Hydrodynamic interaction of microswimmers near a wall. *Phys. Rev. E* **90** (1), 013010.
LI, H. & BOTTO, L. 2024 Hindered settling of a log-normally distributed Stokesian suspension. *J. Fluid Mech.* **1001**, A30.
LIGHTHILL, M.J. 1952 On the squirming motion of nearly spherical deformable bodies through liquids at very small Reynolds numbers. *Commun. Pure Appl. Math.* **5** (2), 109–118.
LIN, Z. & GAO, T. 2019 Direct-forcing fictitious domain method for simulating non-Brownian active particles. *Phys. Rev. E* **100** (1), 013304.
LOVECCHIO, S., CLIMENT, E., STOCKER, R. & DURHAM, W.M. 2019 Chain formation can enhance the vertical migration of phytoplankton through turbulence. *Sci. Adv.* **5** (10), eaaw7879.
MORE, R.V. & ARDEKANI, A.M. 2020 Motion of an inertial squirmer in a density stratified fluid. *J. Fluid Mech.* **905**, A9.
MORE, R.V. & ARDEKANI, A.M. 2021 Hydrodynamic interactions between swimming microorganisms in a linearly density stratified fluid. *Phys. Rev. E* **103** (1), 013109.
MORICHE, M., HETTMANN, D., GARCÍA-VILLALBA, M. & UHLMANN, M. 2023 On the clustering of low-aspect-ratio oblate spheroids settling in ambient fluid. *J. Fluid Mech.* **963**, A1.
NICOLAI, H., HERZHAFT, B., HINCH, E.J., OGER, L. & GUAZZELLI, E. 1995 Particle velocity fluctuations and hydrodynamic self-diffusion of sedimenting non-Brownian spheres. *Phys. Fluids* **7** (1), 12–23.
OMORI, T., KIKUCHI, K., SCHMITZ, M., PAVLOVIC, M., CHUANG, C.-H. & ISHIKAWA, T. 2022 Rheotaxis and migration of an unsteady microswimmer. *J. Fluid Mech.* **930**, A30.
OUILLON, R., HOUGHTON, I.A., DABIRI, J.O. & MEIBURG, E. 2020 Active swimmers interacting with stratified fluids during collective vertical migration. *J. Fluid Mech.* **902**, A23.

https://doi.org/10.1017/jfm.2026.12141 Published online by Cambridge University Press

OUYANG, Z., LIN, Z., YU, Z., LIN, J. & PHAN-THIEN, N. 2022 Hydrodynamics of an inertial squirmer and squirmer dumbbell in a tube. *J. Fluid Mech.* **939**, A32.
PADDING, J.T. & LOUIS, A.A. 2004 Hydrodynamic and Brownian fluctuations in sedimenting suspensions. *Phys. Rev. Lett.* **93** (22), 220601.
PEDLEY, T.J. & KESSLER, J.O. 1992 Hydrodynamic phenomena in suspensions of swimming microorganisms. *Annu. Rev. Fluid Mech.* **24** (1), 313–358.
PEDLEY, T.J. 2016 Spherical squirmers: models for swimming micro-organisms. *IMA J. Appl. Math.* **81**, 488–521.
PENG, Y., LAI, L., TAI, Y.-S., ZHANG, K., XU, X. & CHENG, X. 2016 Diffusion of ellipsoids in bacterial suspensions. *Phys. Rev. Lett.* **116**, 068303.
PHILLIPS, R.J., BRADY, J.F. & BOSSIS, G. 1988 Hydrodynamic transport properties of hard-sphere dispersions. I. Suspensions of freely mobile particles. *Phys. Fluids* **31** (12), 3462–3472.
QI, K., WESTPHAL, E., GOMPPER, G. & WINKLER, R.G. 2022 Emergence of active turbulence in microswimmer suspensions due to active hydrodynamic stress and volume exclusion. *Commun. Phys.* **5** (1), 49.
QIU, J., CUI, Z., CLIMENT, E. & ZHAO, L. 2022*a* Gyrotactic mechanism induced by fluid inertial torque for settling elongated microswimmers. *Phys. Rev. Res.* **4** (2), 023094.
QIU, J., CUI, Z., CLIMENT, E. & ZHAO, L. 2024 Clustering of settling microswimmers in turbulence. *Nonlinear Process. Geophys.* **31** (2), 229–236.
QIU, J., MARCHIOLI, C. & ZHAO, L. 2022*b* A review on gyrotactic swimmers in turbulent flows. *Acta Mechanica Sin.* **38**, 722323.
QUAN, Y., ZHANG, M., YU, Z., LIN, J., XIA, Y. & LIN, Z. 2025 The locomotion of microorganisms in viscoelastic fluids at finite Reynolds numbers. *J. Fluid Mech.* **1020**, A57.
RICHARDSON, J.F. & ZAKI, W.N. 1997 Sedimentation and fluidisation: Part I. *Chem. Engng Res. Des.* **75**, S82–S100.
ROBERTS, A.M. & DEACON, F.M. 2002 Gravitaxis in motile micro-organisms: the role of fore–aft body asymmetry. *J. Fluid Mech.* **452**, 405–423.
RÜHLE, F., ZANTOP, A.W. & STARK, H. 2022 Gyrotactic cluster formation of bottom-heavy squirmers. *Eur. Phys. J. E* **45** (3), 26.
SANDOVAL, M. 2013 Anisotropic effective diffusion of torqued swimmers. *Phys. Rev. E* **87** (3), 032708.
SOKOLOV, A., ARANSON, I.S., KESSLER, J.O. & GOLDSTEIN, R.E. 2007 Concentration dependence of the collective dynamics of swimming bacteria. *Phys. Rev. Lett.* **98** (15), 158102.
UHLMANN, M. & DOYCHEV, T. 2014 Sedimentation of a dilute suspension of rigid spheres at intermediate Galileo numbers: the effect of clustering upon the particle motion. *J. Fluid Mech.* **752**, 310–348.
WANG, S. & ARDEKANI, A. 2012 Inertial squirmer. *Phys. Fluids* **24** (10), 101902.
WANG, S. & ARDEKANI, A.M. 2015 Biogenic mixing induced by intermediate Reynolds number swimming in stratified fluids. *Sci. Rep.* **5** (1), 17448.
WENSINK, H.H., DUNKEL, J., HEIDENREICH, S., DRESCHER, K., GOLDSTEIN, R.E., LÖWEN, H. & YEOMANS, J.M. 2012 Meso-scale turbulence in living fluids. *Proc. Natl Acad. Sci.* **109** (36), 14308–14313.
WU, X.-L. & LIBCHABER, A. 2000 Particle diffusion in a quasi-two-dimensional bacterial bath. *Phys. Rev. Lett.* **84** (13), 3017.
WU, Z., CHEN, Y., MUKASA, D., PAK, O.S. & GAO, W. 2020 Medical micro/nanorobots in complex media. *Chem. Soc. Rev.* **49** (22), 8088–8112.
XIA, Y., LIN, Z., GUO, Y. & YU, Z. 2024 Modelling of filtered drag force for clustered particle-laden flows based on interface-resolved simulation data. *J. Fluid Mech.* **998**, A57.
XIA, Y., LIN, Z. & YU, Z. 2025*a* Modelling mesoscale turbulence in clustered gas–solid flows based on particle-resolved simulation data. *J. Fluid Mech.* **1021**, A6.
XIA, Y., YU, Z., HU, X., ZHU, C. & LIN, Z. 2025*b* Pairwise interactions of active particles in a yield stress fluid. *J. Non-Newtonian Fluid Mech.* **345**, 105486.
XIA, Y., YU, Z., PAN, D., LIN, Z. & GUO, Y. 2022 Drag model from interface-resolved simulations of particle sedimentation in a periodic domain and vertical turbulent channel flows. *J. Fluid Mech.* **944**, A25.
XIA, Y., YU, Z., ZHANG, M., LIN, Z. & OUYANG, Z. 2025*c* Swimming dynamics of a spheroidal microswimmer near a wall. *Phys. Rev. E* **111** (4), 045106.
YIN, X. & KOCH, D.L. 2007 Hindered settling velocity and microstructure in suspensions of solid spheres with moderate Reynolds numbers. *Phys. Fluids* **19** (9), 093302.
YOSHINAGA, N. & LIVERPOOL, T.B. 2018 From hydrodynamic lubrication to many-body interactions in dense suspensions of active swimmers. *Eur. Phys. J. E* **41**, 76.
YU, Z. & SHAO, X. 2007 A direct-forcing fictitious domain method for particulate flows. *J. Comput. Phys.* **227** (1), 292–314.

https://doi.org/10.1017/jfm.2026.12141 Published online by Cambridge University Press

ZHANG, H.-P., BE'ER, A., FLORIN, E.-L. & SWINNEY, H.L. 2010 Collective motion and density fluctuations in bacterial colonies. *Proc. Natl Acad. Sci.* **107** (31), 13626–13630.

ZHANG, M., YU, Z., OUYANG, Z., XIA, Y. & LIN, Z. 2024 Numerical study of collective motion of microswimmers in Giesekus viscoelastic fluids. *J. Non-Newtonian Fluid Mech.* **329**, 105245.

ZÖTTL, A. & STARK, H. 2014 Hydrodynamics determines collective motion and phase behavior of active colloids in quasi-two-dimensional confinement. *Phys. Rev. Lett.* **112** (11), 118101.

https://doi.org/10.1017/jfm.2026.12141 Published online by Cambridge University Press